2021

DYNAMIC BEHAVIOR OF ADDITIVELY MANUFACTURED METAL ALLOYS

Chelsea Fox
University of Rhode Island, cfox@caltech.edu

DYNAMIC BEHAVIOR OF ADDITIVELY MANUFACTURED METAL ALLOYS

BY

CHELSEA FOX

A THESIS SUBMITTED IN PARTIAL FULFILLMENT OF THE

REQUIREMENTS FOR THE DEGREE OF

MASTER OF SCIENCE

IN

MECHANICAL ENGINEERING AND APPLIED MECHANICS

UNIVERSITY OF RHODE ISLAND

2021

MASTER OF SCIENCE IN MECHANICAL ENGINEERING AND APPLIED MECHANICS

OF

CHELSEA FOX

APPROVED:

Thesis Committee:

Major Professor Carl-Ernst Rousseau

Co-Major Professor Arun Shukla

David Taggart

George Tsiatas

Brenton DeBoef
DEAN OF THE GRADUATE SCHOOL

UNIVERSITY OF RHODE ISLAND
2021

ABSTRACT

The dynamic behavior of additively manufactured metal alloys is investigated. For 17-4PH stainless steel (with H1100 heat treatment) and a nickel-copper alloy, the dynamic constitutive behavior is tested at various rates of compressive and tensile loading at both room and high temperatures. Experiments are conducted using an Instron 5582 Universal Tester and a Shimadzu AGX Universal Test Frame for quasi-static compression and tensile tests, respectively, and a Split Hopkinson Pressure Bar for all dynamic tests. An induction coil heating system is used for the high temperature (HT) experiments. Strain rates of 10^{-3} s^{-1} to 10^{4} s^{-1} are studied. At the dynamic strain rate of 2500 s^{-1}, the effects of HT are investigated for temperatures ranging from 22 ºC to 1000 ºC for compressive loading and for temperatures from 22 ºC to 600 ºC for tensile loading. Johnson-Cook models (one for compressive loading and one for tensile loading) are established to determine the dynamic plastic response of the 17-4PH H1100 stainless steel for various strain rates and temperatures.

The dynamic response of additively manufactured nickel-copper alloy corrugated panels is studied using a shock tube. By keeping areal mass density and face sheet dimensions the same for all panels, hexagonal and sinusoidal corrugation geometries are tested to determine the effect of corrugation geometry on shock response. The panels have four layers of corrugation allowing for an equal number of contact points between the corrugations and the face sheets on both the front face (shock side) and back face of the panel, as preliminary tests demonstrated the importance of equal contact. Corrugation buckling and back face panel deflection are tracked using high speed photography and 3D Digital Image Correlation (DIC).

ACKNOWLEDGEMENTS

I would like to acknowledge ONR Award No. N0014-20-1-2040 for the generous support of this work. I would like to thank my advisors Dr. Carl-Ernst Rousseau and Dr. Arun Shukla for their invaluable mentorship throughout my graduate studies at URI. I would also like to thank my DPML colleagues for their excellent research discussion and collaboration. Finally, I would like to thank my parents for their love and support throughout my graduate studies.

PREFACE

This thesis is written in manuscript format. Chapter 1 is the Dynamic Constitutive Behavior of Additively Manufactured 17-4PH Stainless Steel. Chapter 2 is the Dynamic Constitutive Behavior of an Additively Manufactured Nickel-Copper Alloy. Chapter 3 is the Shock Response of Additively Manufactured Nickel-Copper Alloy Corrugated Panels. The research in all three chapters is conducted under Controlled Unclassified Information (CUI) conditions. Chapter 1 has been cleared for public release and has been submitted for publication in the Journal of Dynamic Behavior of Materials. Chapters 2 and 3 are both under preparation for journal submission and are written as a preliminary form of the work without any CUI information. The results of these two chapters will be presented during the defense.

TABLE OF CONTENTS

LIST OF TABLES

LIST OF FIGURES

CHAPTER ONE

Submitted for publication in the Journal of Dynamic Behavior of Materials

Dynamic Constitutive Behavior of Additively Manufactured 17-4PH Stainless Steel

C. Fox[1], C. Tilton[1], C. Rousseau[1]*, A. Shukla[1], C. Sheeley[2], R. Hebert[2]

[1]*Dynamic Photo-Mechanics Laboratory, Department of Mechanical, Industrial & Systems Engineering, University of Rhode Island, Kingston, RI 02881, USA*
[2]*Department of Materials Science & Engineering, University of Connecticut, Storrs, CT 06269, USA*

*Corresponding Author. E-mail address: roussce@uri.edu; Telephone: 401-874-2542

Dynamic Constitutive Behavior of Additively Manufactured 17-4PH Stainless Steel

C. Fox[1], C. Tilton[1], C. Rousseau[1]*, A. Shukla[1], C. Sheeley[2], R. Hebert[2]

[1]*Dynamic Photo-Mechanics Laboratory, Department of Mechanical, Industrial & Systems Engineering, University of Rhode Island, Kingston, RI 02881, USA*
[2]*Department of Materials Science & Engineering, University of Connecticut, Storrs, CT 06269, USA*

*Corresponding Author. E-mail address: roussce@uri.edu; Telephone: 401-874-2542

Abstract

The dynamic constitutive behavior of additively manufactured (AM) 17-4PH stainless steel (SS) was investigated at various rates of compressive and tensile loading at both room and high temperatures. In accordance with common practice in current marine applications, the specimens were heat treated to H1100 condition. Experiments were conducted using an Instron 5582 Universal Tester and a Shimadzu AGX Universal Test Frame for quasi-static compression and tensile tests, respectively, and a Split Hopkinson Pressure Bar for all dynamic tests. An induction coil heating system was used for the high temperature (HT) experiments. Strain rates of 10^{-3} s^{-1} to 10^{4} s^{-1} were studied. At the dynamic strain rate of 2500 s^{-1}, the effects of HT were investigated for temperatures ranging from 22 ºC to 1000 ºC for compressive loading and for temperatures from 22 ºC to 600 ºC for tensile loading. The results show strain rate and temperature dependencies. Two Johnson-Cook models (one for compressive loading and one for tensile loading) were established to determine the dynamic plastic response of the material for various strain rates and temperatures.

Keywords

additively manufactured; stainless steel; Split-Hopkinson pressure bar, high temperature; Johnson-Cook model

Introduction

A widely used alloy, traditionally manufactured 17-4PH SS is a common and practical choice for many industries, including aerospace, chemical and food processing, due to its high strength, good corrosion resistance and good mechanical properties at high temperatures. This metal can also be easily heat treated to suit a variety of applications [1]. With the recent advent of additive manufacturing, which can fabricate complex geometries as well as reduce waste and save money, much research has been conducted to determine if AM 17-4PH SS is a suitable replacement for traditionally manufactured 17-4PH SS. Cheruvathur et al. (2016) analyzed the effect of post-processing heat treatment on the microstructure of AM 17-4PH SS, noting that the as-printed material often has a dendritic structure with a large percentage of austenite. Through homogenization heat-treatment, they were able to obtain a microstructure with 90% martensite and only 10% austenite, which more closely resembles that of wrought 17-4PH SS than the as-built condition [2]. Lum et al. (2017) investigated the effect of additive manufacturing on the material properties of 15-5PH stainless steel, a similar material to 17-4PH SS, and found that the additive manufacturing process left behind unmelted regions and a small percentage of austenitic structure [3]. Rafi et al. (2014) examined the effect of argon and nitrogen atmospheres during the laser sintering process to determine the effects and also found that post-process heat treatment is required to obtain better tensile material

properties, as the phase content is greatly influenced by multiple factors besides the AM atmosphere [4]. Multiple studies have been conducted to examine the fatigue and tensile properties of AM 17-4PH SS for a variety of heat treatments [5-7]. Yadollahi et al. also noted that, during tensile testing, the build orientation of the AM 17-4PH SS affected the material properties and concluded that defects such as pores from entrapped gas, as well as regions where the 17-4PH powder did not melt or fuse sufficiently, played a noticeable role in why the AM material was inferior to its wrought version [7]. However, to the best of the authors' knowledge, no studies have been conducted on the high temperature dynamic characterization of AM 17-4PH SS. Therefore, this paper will evaluate the thermo-mechanical response of this material and will provide the Johnson-Cook model parameters to describe obtained results.

Experimental Details

Additive Manufacturing of Test Specimens

Samples are additively manufactured using a 3DSystems ProX300 machine with powder supplied by North American Höganäs High Alloys LLC. This powder is vacuum melted and then gas-atomized in argon gas. A typical composition is shown in Table 1.

Table 1 Chemical composition of 17-4PH powder in weight percentages, balance is iron

Cr	**Ni**	**Cu**	**Nb+Ta**	**C**	**Mn**	**N**	**O**	**P**	**S**	**Si**
15.7	3.42	3.98	0.31	0.07	0.08	0.01	0.05	<0.01	0.004	<0.1

Argon is used to operate the ProX300 machine. During the additive manufacturing process, the oxygen level in the build chamber is limited to less than 1000 ppm. The laser settings are summarized in Table 2. The powder layer height before laser melting is approximately 50 μm.

Table 2 Laser settings use for ProX300 machine

Laser Speed (mm/s)	Laser Power (W)	Hatch Spacing (μm)
1,200	140	50

Following the additive manufacturing process, samples are solution heat-treated in air at 1,038 °C for one hour, air-cooled to room temperature, and subsequently aged at 593 °C for four hours to achieve an H1100 condition. The microstructure of a longitudinal section of both an AM (A) and a wrought sample (B) in H1100 condition is shown in Fig. 1.

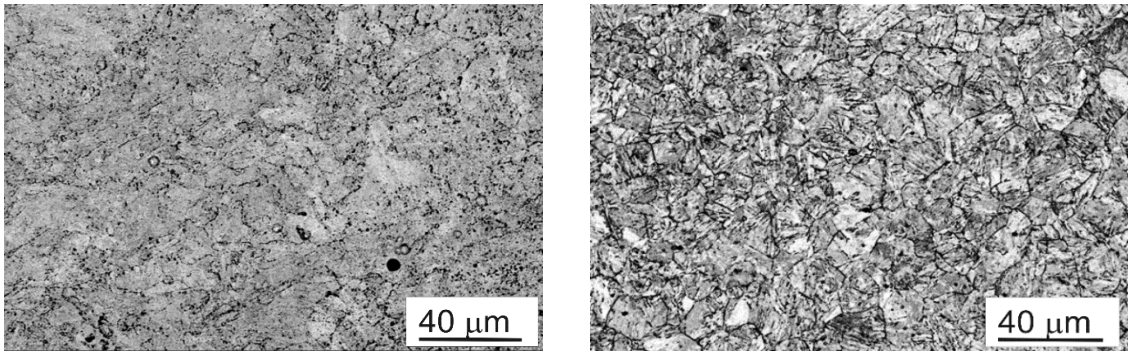

(A) **(B)**

Fig. 1 Microstructure of additively manufactured 17-4PH samples in H1100 condition (A) and wrought 17-4PH in H1100 condition (B)

In the as-built condition, additively manufactured samples reveal significant microstructural differences to their wrought counterparts: Extended columnar grains are typically observed for additively manufactured samples while wrought samples reveal typically an equiaxed martensitic microstructure. Solution heat treatment then occurs in a temperature range that establishes an austenitic microstructure. During the subsequent air cooling, the austenite then transforms to martensite. The final ageing treatment then induces nanoscale precipitates that significantly contribute to the strength of the heat-treated alloy. Despite the significant microstructure differences between as-built additively manufactured sample and wrought sample, the heat-treatment steps induced comparable microstructures in prior work [8]. As in the prior work, the comparison between the two images in Fig. 1 suggests a slightly smaller grain size for the additively manufactured sample than for the wrought counterpart. Figure 1A reveals second phase particles at grain boundaries and it is likely that these particles are carbides or inclusions that inhibit grain growth of the additively manufactured sample during the ageing treatment.

Compressive Quasi-static Characterization

An Instron 5582 Universal Tester is used to determine the compressive quasi-static behavior of H1100 AM 17-4PH SS at RT. The specimen dimensions (see Table 3) and testing procedure are determined from ASTM standard E9-19. During testing a compression rate 1.524 mm/min is used to achieve a strain rate of 10^{-3} s^{-1} up to 25% strain. To reduce interfacial friction between the Instron compression platens and the specimen, molybdenum disulfide is used as a lubricant.

Compressive Dynamic Characterization

A Split Hopkinson Pressure Bar (SHPB) is used to determine the dynamic behavior of H1100 AM 17-4PH SS at 22° C, which will be referred to as RT, and at HT's of 400 °C, 600 °C, 800 °C and 1000 °C. Strain rates varying from 10^3 to 10^4 are investigated. The SHPB is comprised of an incident bar, a transmitted bar and a striker bar, all made of 350 maraging steel, as shown in Fig. 2. These bars are aligned along a horizontal axis to ensure uniform specimen deformation and one-dimensional elastic waves during testing.

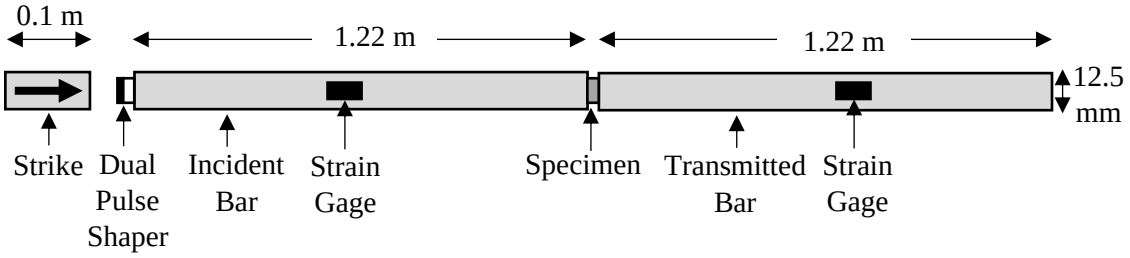

Fig. 2 SHPB compressive loading configuration

Before a test, the cylindrical specimen is positioned between the incident and transmitted bars. The specimen geometry is determined from length to diameter ratios chosen to ensure a state of uniaxial stress, minimal interface friction and reduced specimen inertia in both the radial and longitudinal directions. Table 3 details the specimen dimensions used in this study.

Table 3 Compression cylinder specimen details

Strain Rate (s^{-1})	Quasi-static	1000	2500	5000	10000
Diameter (mm)	12.5	6.4	6.4	3.8	3.8
Thickness (mm)	25.4	4.2	4.2	2.5	2.5
Temperature (°C)	22	22	22, 400, 600, 800, 1000	22	22

To minimize interfacial friction and prevent barreling, the specimen is well lubricated with molybdenum disulfide for RT tests and with boron nitride for HT tests. To conduct the SHPB test, a gas gun is mounted at the end of the incident bar and fires the striker bar, causing it to impact the incident bar. The striker velocity determines the magnitude of the stress wave, while the striker length determines the pulse length. A pulse shaper is positioned between the striker and the incident bar to optimize the strain profile. This pulse shaper allows for stress equilibrium and constant strain rate in the specimen for the duration of the test. In order to optimize the experiments, a dual copper/steel pulse shaper was used for all strain rates, with the copper (0.375" diameter (9.5 mm), 0.05" length (1.3 mm)) positioned before the steel (0.375" diameter (9.5 mm), 0.25" length (6.4 mm)), which is affixed to the striker end of the incident bar with petroleum grease. This dual pulse shaper decreases the sharpness of the initial rise time and shapes the compressive pulse to match that of the specimens [9]. Additional details about the SHPB can be obtained from Kolsky [10]. Axial strain gages mounted on the incident and transmitted bars connect to a dynamic signal conditioning amplifier and oscilloscope system that record the experimental data. Two strain gages are mounted on each bar at least one striker length from the specimen to prevent superposition of the stress waves and at 180^{o} offsets to negate possible bending of the bars. Each strain gage is connected in a quarter Wheatstone bridge configuration. A

typical strain profile is shown in Figure 3. It is clear that the dual pulse shaping technique reduces the Pochhammer-Chree waves in the incident and subsequent pulses. Thus, from the strain measured in the incident and transmitted bars, the specimen strain and strain rates can be determined.

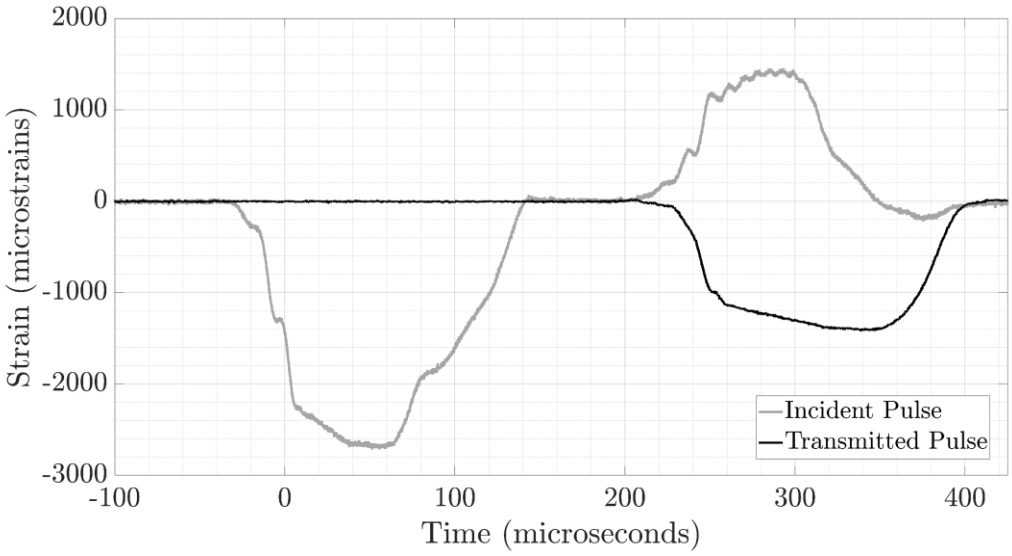

Fig. 3 Real time incident and transmitted strain data pulses for 10^3 s^{-1}

From the strain data, using one-dimensional wave theory, the engineering strain rate, engineering stress and engineering strain can be determined from the following equations, respectively,

$$\dot{\varepsilon}(t) = \frac{-2C_b}{L_s}\varepsilon_r(t), \tag{1}$$

$$\sigma_s(t) = E_b \frac{A_b}{A_s}\varepsilon_t(t), \tag{2}$$

$$\varepsilon_s(t) = \frac{-2C_b}{L_s}\int_0^t \varepsilon_r(t)dt, \tag{3}$$

where C_b is the longitudinal wave speed in the incident and transmitted bars ($C_b = \sqrt{E_b/\rho_b}$, where E_b is the elastic modulus of the incident and transmitted bars and ρ_b is the their

density), L_s is the thickness of the specimen, ε_r is the reflected bar strain, A_b is the cross-sectional area of the bars, A_s is the cross-sectional area of the specimen, ε_i is the incident bar strain and ε_t is the transmitted bar strain [11]. In SHPB tests, for ductile materials such as metals, a constant true strain rate is difficult to achieve, thus the engineering strain rate is typically considered. However, it is important to use the true stress and true strain rather than the engineering stress and strain because adiabatic heating can contribute to softening of the material, thereby negating the strain hardening, which may be inaccurately represented by engineering stress-strain curves [9]. Thus, the true stress and true strain may be determined from the following equations, respectively,

$$\sigma_t(t) = \sigma_s(t)(1 - \varepsilon_s(t)), \tag{4}$$

$$\varepsilon_t(t) = -\ln(1 - \varepsilon_s(t)). \tag{5}$$

It is also important to verify the force equilibrium at the specimen interfaces with the incident (front face, F_i) and transmitted (back face, F_t) bars from the following equations, respectively, in order to have a valid SHPB test.

$$F_i(t) = A_b E_b(\varepsilon_i(t) + \varepsilon_r(t)) \tag{6}$$

$$F_t(t) = A_b E_b \varepsilon_t(t) \tag{7}$$

An example of the force equilibrium check can be seen in Fig. 4. The force-time histories of the front and back faces of the specimen indicate that the specimen is experiencing equilibriated axial stresses during the dynamic loading for the time duration specified.

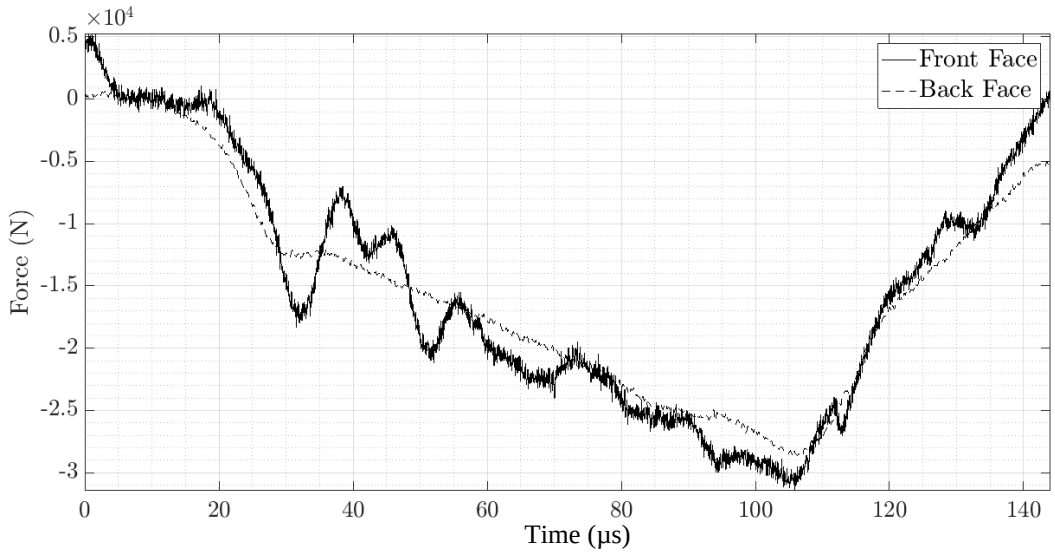

Fig. 4 Force equilibrium at specimen-bar interface for 10^3 s^{-1}

For the HT tests, the SHPB setup is modified to include an induction coil heating system placed over the specimen, as shown in Fig. 5 [12]. Two pumps circulate water through two independent copper coils that are positioned over the ends of the incident and transmitted bars that are in contact with the specimen. This is to prevent a heat gradient in the bars, which would affect their modulus, and thus the wave speed, and to protect the heat-sensitive strain gages. A tungsten carbide insert is placed between the specimen and the incident bar and another between the specimen and the transmitted bar to additionally prevent heating of the bars. The impedance of the tungsten carbide inserts is calculated so as to prevent the compressive stress wave from being altered before reaching the specimen. Therefore, the inserts are 50% smaller in diameter than the incident and transmitted bars. In order to reach the desired experimental temperature in the specimen, calibration experiments are first conducted to determine the relation between induction heating time at certain amperage levels and desired temperature. The calibration relation is developed

by spot welding a chromel-alumel thermocouple onto a calibration specimen and its temperature is monitored until the desired temperature is reached and maintained.

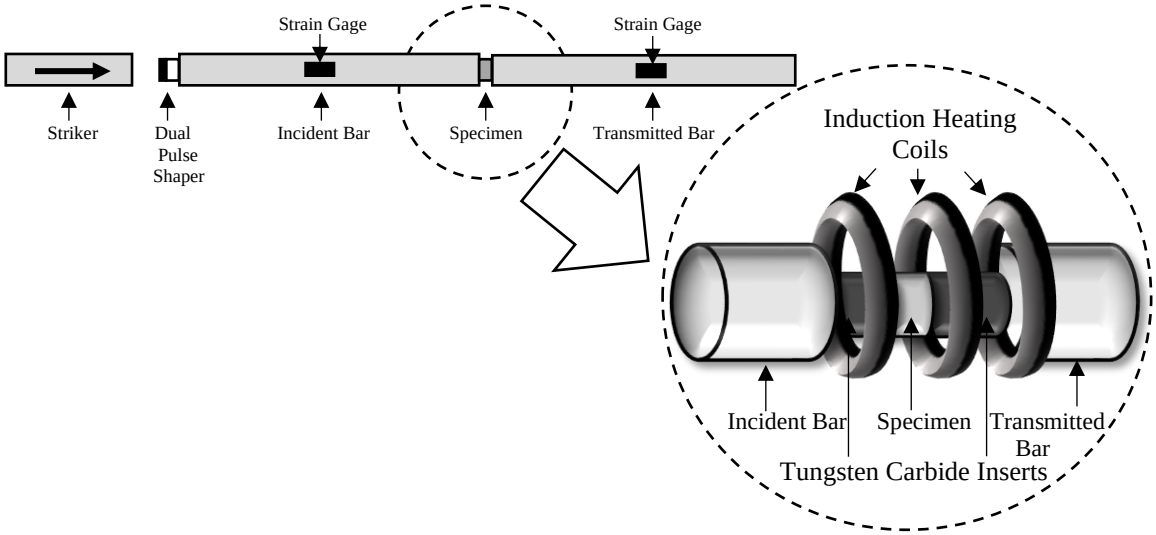

Fig. 5 High temperature compressive SHPB configuration

Tensile Quasi-static Characterization

A Shimadzu AGX Universal Test Frame is used to determine the tensile quasi-static behavior of H1100 AM 17-4PH SS at room temperature. The specimen dimensions and testing procedure are determined from ASTM standard E8. Strain is recorded using a 1 megapixel camera at a frame rate of 10 fps and a random speckle pattern is applied to the specimen so that 2D Digital Image Correlation could be used to measure strain in the vertical direction.

Tensile Dynamic Characterization

A tensile SHPB setup is used to determine the tensile dynamic behavior of H1100 AM 17-4PH SS at RT and at HT's of 400 ºC and 600 ºC [13]. Strain rates on the order of magnitude

10^3 are investigated. The tensile SHPB is comprised of an incident bar with a flange on one end, a transmitted bar and a striker, all made of 350 maraging steel, as shown in Fig. 6. These bars are aligned along a horizontal axis to ensure uniform specimen deformation and one-dimensional elastic waves during testing. To hold the specimen, one end of both the incident and transmitted bars have a threaded section, into which the specimen is threaded, leaving only the gage section of the specimen between the two bars. The specimen details are also shown in Fig. 6. To conduct a test, the striker is fired from a gas gun positioned over the incident bar, causing the striker to impact the flange on the end of the incident bar, generating a tensile wave that propagates down to the specimen. The same strain gage configuration and data acquisition system described for compression are used to measure the elastic deformation of the incident and transmitted bars, which allow for calculation of the specimen's stress and strain responses. In order to optimize the tensile tests, much like in the case of compression, a dual pulse shaper is used; however, this time, it is positioned between the striker and the incident flange. It consists of the same copper/steel combination as in the case of compression, but both of the components are now rings that fit over the incident bar and are positioned against the flange. The copper pulse shaper has inner diameter 25.4 mm, outer diameter 38.1 mm, thickness 1.3 mm, and the steel has inner diameter 21.3 mm, outer diameter 38.1 mm, and thickness 2.8 mm.

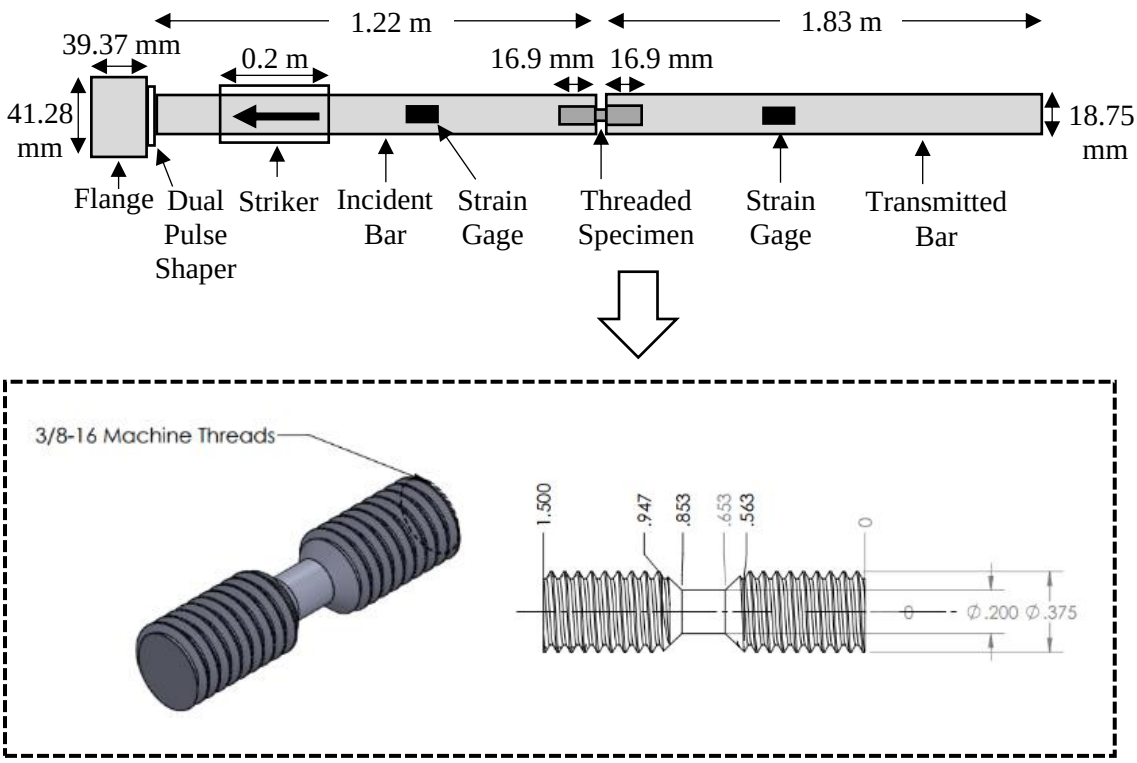

Fig. 6 SHPB tensile loading configuration and specimen details

The one-dimensional wave theory used for compression (Eq.'s 1, 2 and 3) remains valid [12]. However, Eq.'s 4 and 5 must be modified to describe tensile behavior. Thus, the true stress and strain may be described as

$$\sigma_t(t) = \sigma_s(t)(1 + \varepsilon_s(t)), \tag{8}$$

$$\varepsilon_t(t) = \ln(1 + \varepsilon_s(t)). \tag{9}$$

As in the case of compressive tests, during tensile SHPB tests, force equilibrium verification is undertaken, validating the use of Eq.'s 6 and 7. Figure 7 shows the strain-time history for a representative tensile experiment conducted at 1000 s^{-1}. From the figure, it is clear that the specimen dimensions and dual pulse shaping technique mitigates noise and ringing in the signal.

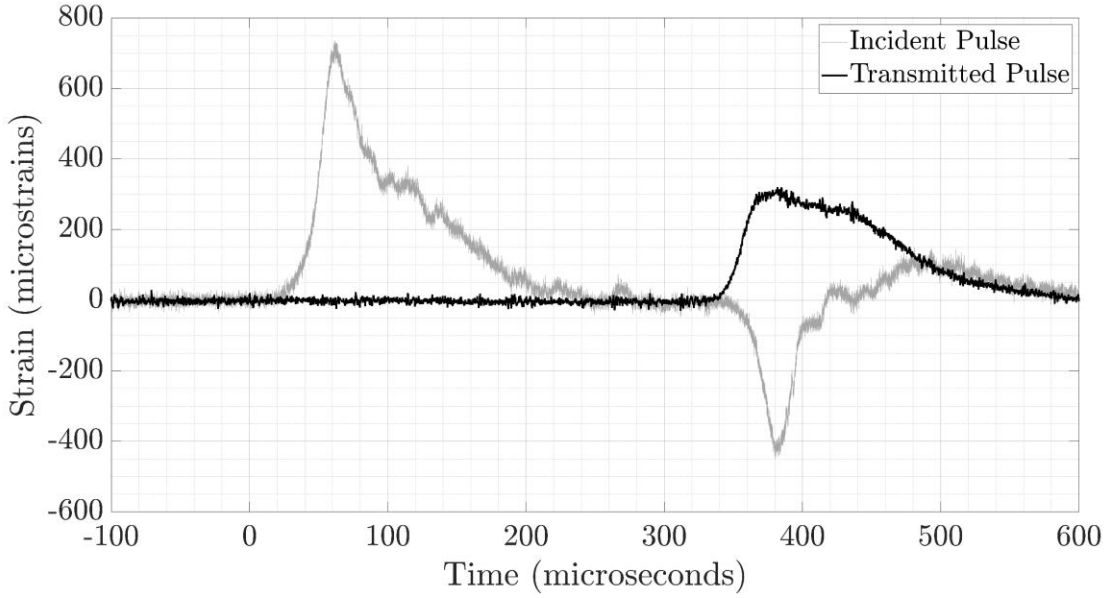

Fig. 7 Real time incident and transmitted strain data pulses for 10^3 s^{-1} in tension

For the HT tests, the tensile SHPB setup is modified to include an induction coil heating system placed over the specimen, as in the case of the HT compressive setup. Similarly, two pumps circulate water through two independent copper coils that are positioned over the ends of the incident and transmitted bars that are in contact with the specimen. The same calibration method as described in the compressive HT configuration is used to determine the correct settings and time to reach the required temperature in the specimen before a test is conducted. Due to the fact that the tensile specimens are threaded into the incident and transmitted bars, boron nitride is used a lubricant to ensure that the specimens could be removed after testing without damage to the threaded sections of the bars. The threaded nature of the tensile SHPB also determined that 600 ºC was the upper testing limit before bars began experiencing a level of heating that could no longer be controlled by the copper cooling coils, thus altering the modulus of the bars [14].

Experimental Results

Compressive Dynamic Constitutive Response (Room Temperature)

The compressive dynamic material properties of H1100 AM 17-4PH SS were determined for four different dynamic strain rates (1000 s^{-1}, 2500 s^{-1}, 5000 s^{-1} and 10000 s^{-1}) at RT and each experiment was conducted five times for consistency. For this data, and all subsequent data, the yield strength is taken as the 0.2% offset. In Fig. 8, the RT true stress-true strain curves are plotted for one representative trial for the dynamic strain rates of 1000 s^{-1}, 2500 s^{-1}, 5000 s^{-1} and 10000 s^{-1} and for the quasi-static strain rate (10^{-3} s^{-1}). Figure 8 shows that H1100 AM 17-4PH SS is strain rate dependent in compression from quasi-static to dynamic strain rates, since yield strength increases by 8% as the strain rate increases from 10^{-3} s^{-1} to 1000 s^{-1}. A 12% increase in yield strength is observed as the strain rate increases from 10^{-3} s^{-1} to 2500 s^{-1}, a 27% increase is observed from 10^{-3} s^{-1} to 5000 s^{-1}, and a 31% increase is observed from 10^{-3} s^{-1} to 10^{4} s^{-1}. The average dynamic compressive flow stresses are approximately 50 MPa, 100 MPa, 150 MPa, and 225 MPa greater than the average quasi-static compressive flow stress, respectively for the 1000 s^{-1}, 2500 s^{-1}, 5000 s^{-1} and 10000 s^{-1} strain rates.

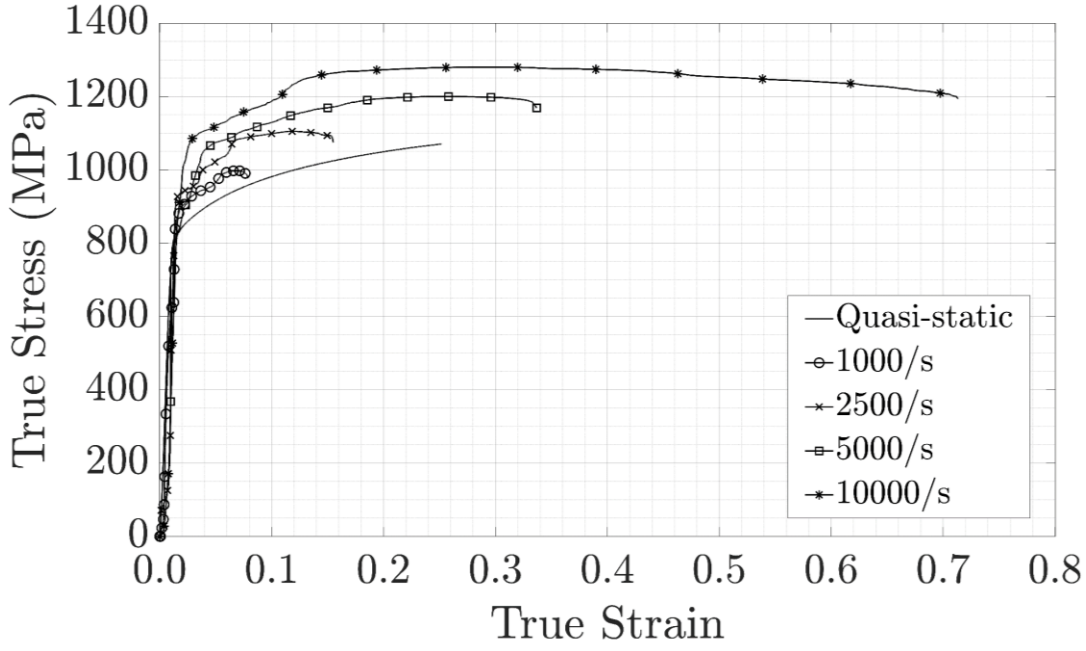

Fig. 8 True compressive stress-strain curves for room temperature dynamic loading

Compressive Dynamic Constitutive Response (High Temperature)

The compressive dynamic material properties of H1100 AM 17-4PH SS were determined at 2500 s^{-1} for five different temperatures (RT, 400 °C, 600 °C, 800 °C and 1000 °C) and each experiment was conducted five times for consistency. The corresponding true stress-true strain curves are plotted in Fig. 9 for one representative trial. From this figure, it is clear that the compressive material behavior is temperature dependent, as the yield stress and flow stress decrease as the temperature increases. From RT to 400 °C, the yield strength decreases by 27%, while the average flow stress decreases by 325 MPa. From RT to 600 °C, the yield strength decreases by 67%, while the average flow stress decreases by 600 MPa. From RT to 800 °C, the yield strength decreases by 65%, while the average flow stress decreases by 700 MPa. Finally, from RT to 1000 °C, the yield strength decreases by

75%, while the average flow stress decreases by 775 MPa. It is also clear that the relation between temperature and yield stress is not linear, as the yield stresses for 600 °C and 800 °C are similar.

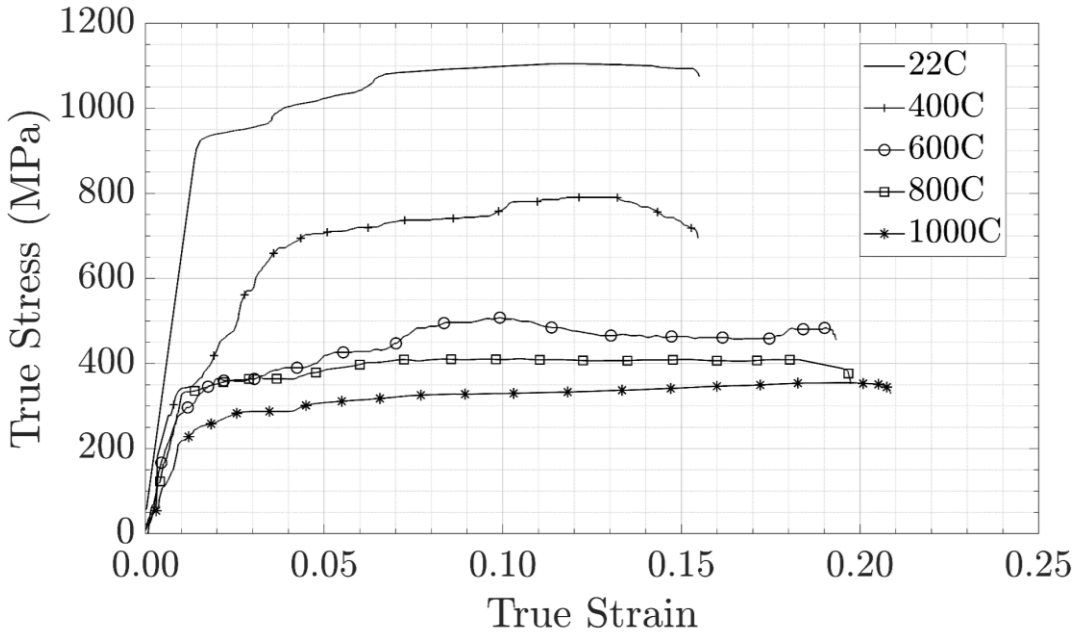

Fig. 9 True compressive stress-strain curves for high temperature dynamic loading (2500 s^{-1})

The experimental stress-strain data of the AM material in compression approximately matches reported literature values for wrought 17-4PH in tension. AK Steel, indeed, reported values for 17-4PH of 790 MPa engineering yield stress for sheet and strip in the H1100 condition and 965 MPa ultimate tensile strength for minimum material specification at room temperature. At 399 °C and for the H1150 condition, a yield stress value was reported of 765 MPa and an ultimate tensile strength of 800 MPa [1].

Tensile Dynamic Constitutive Response (Room Temperature)

The tensile dynamic material properties of H1100 AM 17-4PH SS were determined for three different dynamic strain rates (1000 s^{-1}, 2500 s^{-1} and 5000 s^{-1}) at room temperature and each experiment was conducted five times for consistency. In Fig. 10, the room temperature true stress-true strain curves are plotted for one representative trial for the dynamic strain rates of 1000 s^{-1}, 2500 s^{-1} and 5000 s^{-1} and for the quasi-static strain rate of 10^{-3} s^{-1}. Figure 10 shows that H1100 AM 17-4PH SS is strain rate dependent in tension from quasi-static to dynamic strain rates, since yield strength increases by 50% as the strain rate increases from 10^{-3} s^{-1} to 1000 s^{-1}. A 62% increase in yield strength is observed as the strain rate increases from 10^{-3} s^{-1} to 2500 s^{-1} and a 73% increase is observed from 10^{-3} s^{-1} to 5000 s^{-1}. The average dynamic tensile flow stresses are approximately 325 MPa, 400 MPa and 475 MPa, greater than the average quasi-static tensile flow stress, respectively for the 1000 s^{-1}, 2500 s^{-1} and 5000 s^{-1} strain rates. The specimens all broke during testing at very low strains, indicating brittle failure. The strains to failure were approximately 2.6%, 3.3% and 3.9% for the dynamic strain rates of 1000 s^{-1}, 2500 s^{-1} and 5000 s^{-1}, respectively, while the quasi-static strain to failure was only approximately 1.2%. At dynamic strain rates, it is postulated that adiabatic heating softened the material, resulting in higher strain to failure values than were seen in quasi-static, thus indicating that the material is strain rate sensitive. It is also postulated that the porosity in the material leads to lower failure stresses and strains. This effect seems to be more dominant in quasi-static tensile failure of this material, where a yield stress of 600 MPa (consistent over five specimens tested) compares poorly with a value of 790 MPa for the wrought material [1].

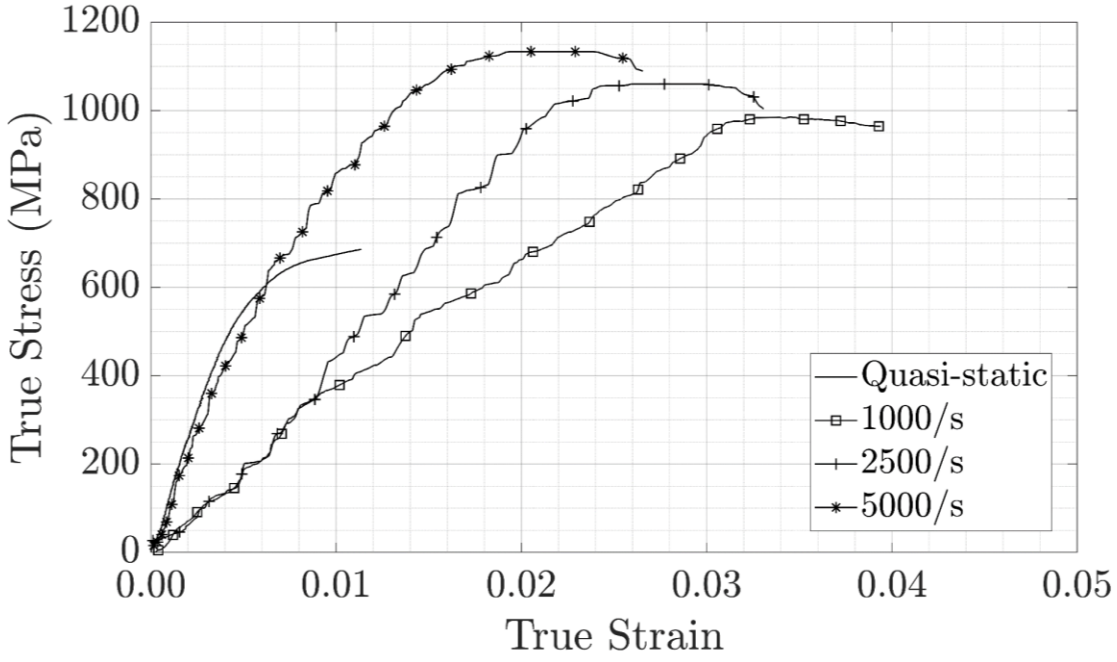

Fig. 10 True tensile stress-strain curves for room temperature dynamic loading

Tensile Dynamic Constitutive Response (High Temperature)

The tensile dynamic material properties of H1100 AM 17-4PH SS were determined at 2500 s^{-1} for three different temperatures (RT, 400 °C and 600 °C) and each experiment was conducted five times for consistency. The corresponding true stress-true strain curves are plotted in Fig. 11 for one representative trial. From this figure, it is clear that the tensile material behavior is temperature dependent, as the yield stress and flow stress decrease as the temperature increases. From RT to 400 °C, the yield strength decreases by 5%, while the average flow stress decreases by 100 MPa. From RT to 600 °C, the yield strength decreases by 20%, while the average flow stress decreases by 200 MPa. It can also be seen that the true plastic strain increases as temperature increases, indicating an increase in ductility before specimen failure, as all specimens broke during testing. The strains to failure were approximately 3.3%, 4.2% and 5% for RT, 400 °C and 600 °C, respectively.

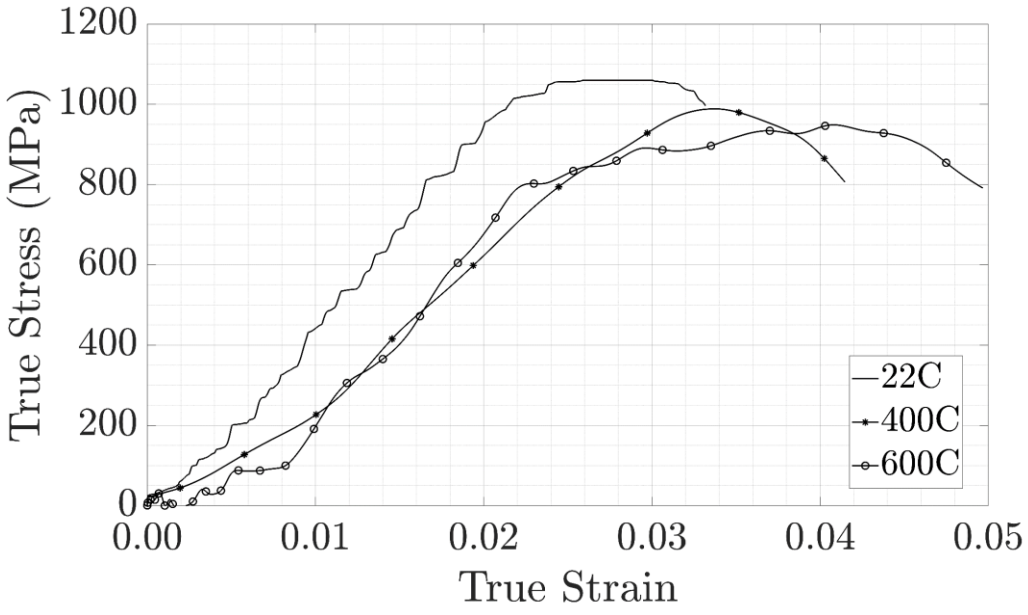

Fig. 11 True tensile stress-strain curves for high temperature dynamic loading (2500 s^{-1})

Modeling Analysis

Johnson-Cook Constitutive Model

The Johnson-Cook constitutive model provides an effective method of predicting the plastic response of materials subjected to HT, high strain rates and large deformations [15]. This empirical model is widely used in the characterization of metals due to its simple and comprehensive form. The model states that the flow stress may be described as

$$\sigma = (A + B\varepsilon_p^n)(1 + Cln\left(\frac{\dot{\varepsilon_p}}{\dot{\varepsilon}_{ref}}\right)(1-(T^*)^m), \quad (10)$$

where σ is the flow stress, A is the yield stress at the reference strain rate, B and n are strain hardening parameters, ε_p is the plastic strain, C is the strain rate parameter, $\dot{\varepsilon_p}$ is the plastic

strain rate, $\dot{\varepsilon}_{ref}$ is the reference strain rate, m is the thermal softening parameter and T^* is the normalized temperature and can be described as

$$T^* = \frac{T - T_{ref}}{T_{melt} - T_{ref}}, \tag{11}$$

where T_{ref} is the reference temperature (RT), T_{melt} is the melting temperature (1400 °C) and T is the experimental temperature.

Determination of Model Parameters for Compressive Loading

The Johnson-Cook model requires five model parameters to effectively describe the plastic response of metals. Parameter A is the yield stress of the material at the reference strain rate, which is commonly defined as the quasi-static strain. However, in order to fit this model to the compressive dynamic strain rates more effectively, the strain rate of 1000 s^{-1} is used as the reference strain rate for this case. Thus, the yield stress at the 0.2% strain offset from the reference strain rate true stress-strain plot is taken. Once parameter A has been determined, parameters B and n may be found. At the reference temperature (RT) and reference strain rate, the Johnson-Cook model may be simplified as

$$ln(\sigma - A) = nln(\varepsilon_p) + ln(B), \tag{12}$$

and a linear regression may be used to fit the quasi-static data to determine the slope, n, and the y-intercept, ln(B). Once A, B and n have been determined, C may be found. Using dynamic SHPB results for strain rates of 1000 s^{-1}, 2500 s^{-1}, 5000 s^{-1} and 10000 s^{-1} at the reference temperature, the Johnson-Cook model may be simplified as

$$\frac{\sigma}{(A + B\varepsilon^n)} = Cln\left(\frac{\dot{\varepsilon_p}}{\dot{\varepsilon}_{ref}}\right) + 1, \tag{13}$$

and again a linear regression may be used to calculate *C*, given a y-intercept of 1. Because the linear regression is unable to completely capture all of the data from the various strain rates, as the resulting plot from Eq. 13 is non-linear, an average value of *C* is obtained. Finally, to determine the value of *m*, experimental data at a strain rate of 2500 s^{-1} and temperatures ranging from RT to 1000 ºC are used. At the given strain rate, the Johnson-Cook model may be simplified as

$$ln\left(1-\frac{\sigma}{(1+Cln\left(\frac{\dot{\varepsilon_p}}{\dot{\varepsilon}_{ref}}\right))(A+B\varepsilon_p^n)}\right)=mln(T^*), \tag{14}$$

and a linear regression may be used to find the slope, *m*. The final step is to optimize the five parameters, given that the experimental data did not provide exact linear relations during their determination. As such, the model may predict some experiments very well with little relative error, while other predictions may be less accurate. Thus, it is important to minimize the error between the model and all experimental data [12]. This is accomplished using the following relation as described by

$$Error=\frac{1}{N}\sum_{i=1}^{N}\left|\frac{\sigma_{exp}^i-\sigma_p^i}{\sigma_{exp}^i}\right|x100\%, \tag{15}$$

where σ_{exp} is the experimental flow stress, σ_p is the predicted flow stress and *N* is the number of data points. The result of this optimization is that by decreasing the parameter *A* to 635, which is below the yield stress for the reference strain rate, the model better predicts the shape of the true stress-strain curves with larger errors at low strain, but with smaller errors at higher strain. The parameters for the H1100 AM 17-4PH SS under compressive loading may be found in Table 4.

Table 4 Johnson-Cook model parameters for compressive loading

Parameter	***A* (MPa)**	***B* (MPa)**	***C***	***n***	***m***
Value	635	500	0.08	0.12	1.02

Determination of Model Parameters for Tensile Loading

The method described in the previous section was used to determine the Johnson-Cook model parameters for tensile loading of H1100 17-4PH SS. Once again, the reference strain rate chosen was 1000 s^{-1} and the same optimization was conducted using Eq. 15. The Johnson-Cook model parameters for H1100 17-4PH SS may be found in Table 5.

Table 5 Johnson-Cook model parameters for tensile loading

Parameter	***A* (MPa)**	***B* (MPa)**	***C***	***n***	***m***
Value	935	100	0.08	0.12	1.99

Johnson-Cook Model Comparison with Experimental Data for Compressive Loading

The comparative results of the Johnson-Cook compression modeling versus the corresponding experimental data are shown in Fig. 12. The elastic region is not considered, while the plastic region is shown, as the model only predicts stress in that region. Table 6 gives the average relative error between the model and the experimental data using Eq. 15. For all RT strain rates, the model predicts well, with less than 7% average relative error for all cases. Additionally, the model predicts better for lower strain rates, as the average relative errors for 1000 s^{-1} and 2500 s^{-1} are only 1.26 and 1.86%, respectively, while the average relative error for 10000 s^{-1} is 6.34%. The model also

predicts well for HT cases, with an exception for the intermediate temperatures of 600 °C and 800 °C. For the 400 °C case, there is an average relative error of 4.98% between the model and experimental data, while for the 1000 °C case, there is an average relative error of 8.64%. However, for the 600 °C and 800 °C cases, there are average relative errors of 34.45% and 23.47%, respectively. At these two temperatures, the experimental yield stresses and flow stresses of the material are very similar. Thus, the model, which uses an exponential term, the parameter, *m*, to describe the effect of increasing temperature on the stress, cannot accurately account for this plateauing behavior and the results display a significant average relative error.

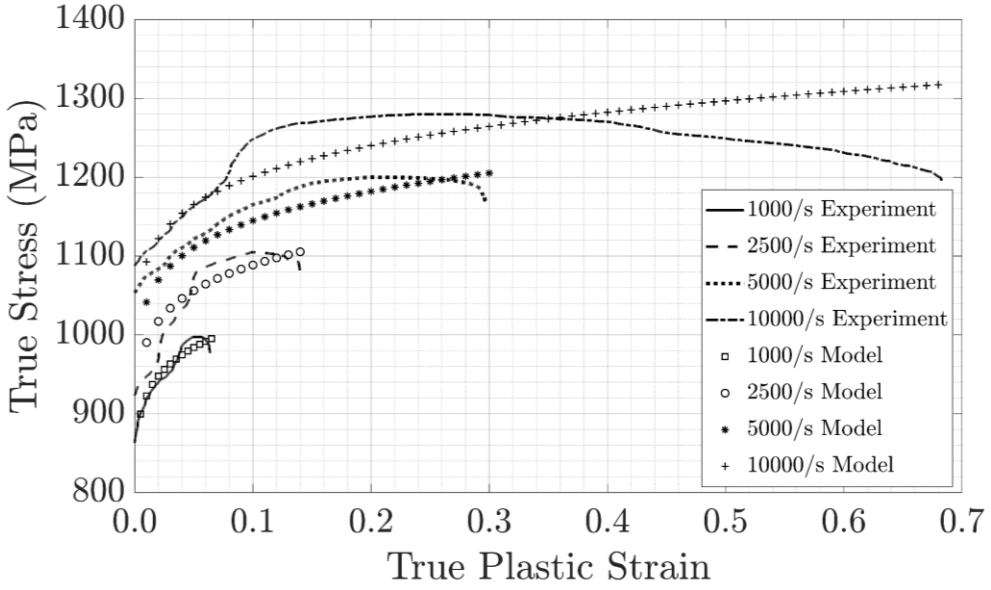

(A)

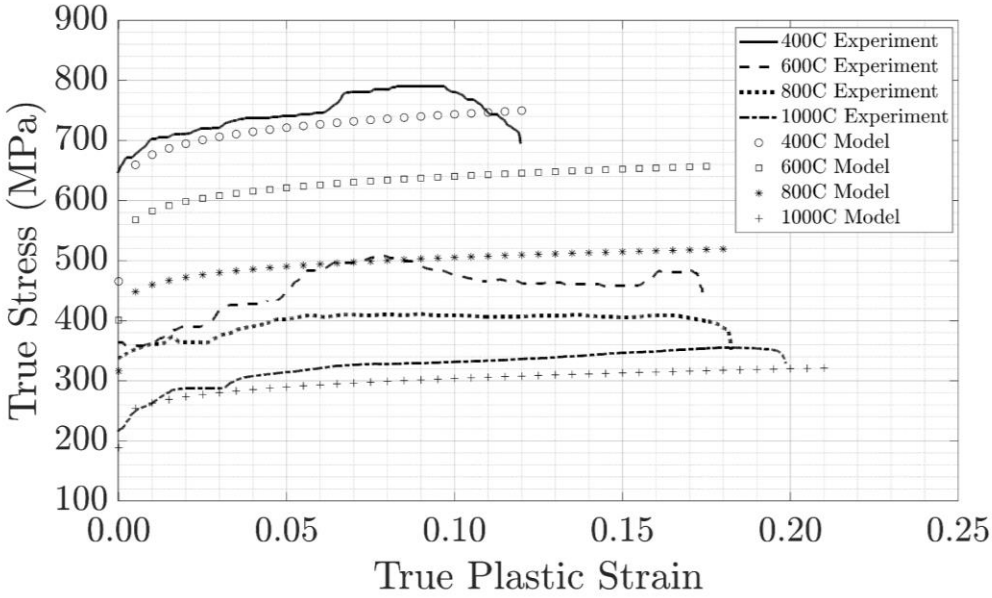

(B)

Fig. 12 Johnson-Cook compressive loading model comparison with experimental data, RT comparison (A) HT comparison (B)

Table 6 Johnson-Cook compressive loading model error analysis

Strain Rate (s^{-1})	Temperature (°C)	Average Relative Error (%)
1000	RT	1.26
2500	RT	1.86
2500	400	4.98
2500	600	34.45
2500	800	23.47
2500	1000	8.64
5000	RT	2.14
10000	RT	6.34

Johnson-Cook Model Comparison with Experimental Data for Tensile Loading

The comparative results of the Johnson-Cook tensile modeling versus the corresponding experimental data are shown in Fig. 13. As before, only the plastic region is shown. Table 7 gives the average relative error between the model and the experimental data using Eq. 15. For all RT strain rates, the model predicts well, with less than 10% average relative error for all cases. Additionally, the model predicts better for lower strain rates, as the average relative errors for 2500 s^{-1} and 5000 s^{-1} are only 4.38% and 5.89%, respectively, while the average relative error for 1000 s^{-1} is 3.74%. The model also predicts well for HT cases. For the 400 °C case, there is an average relative error of 7.31% between the model and experimental data, while for the 600 °C case, there is an average relative error of 5.34%.

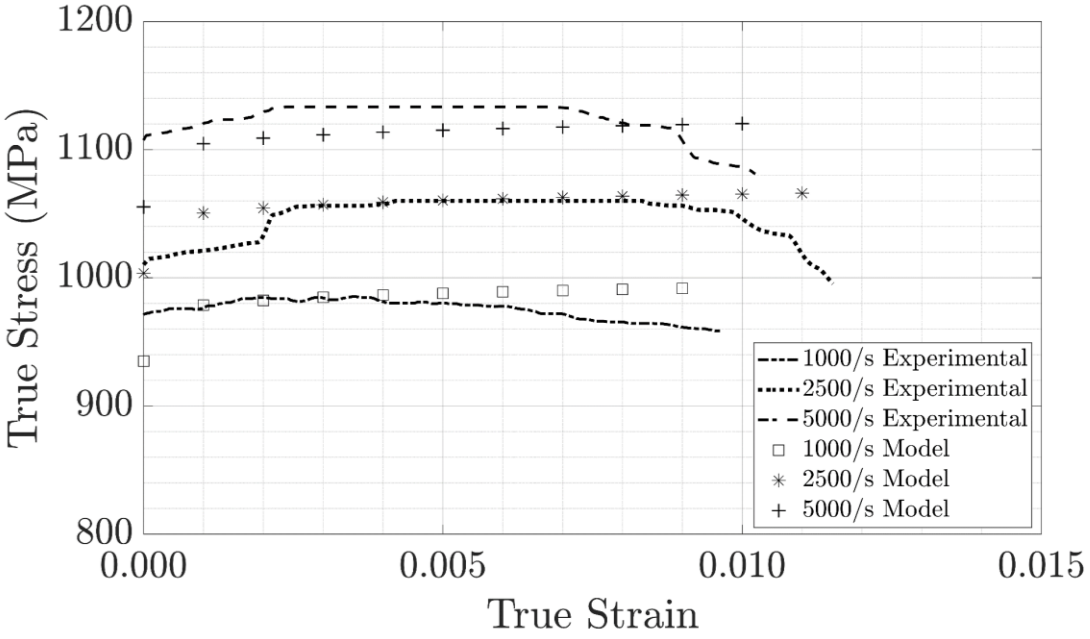

(A)

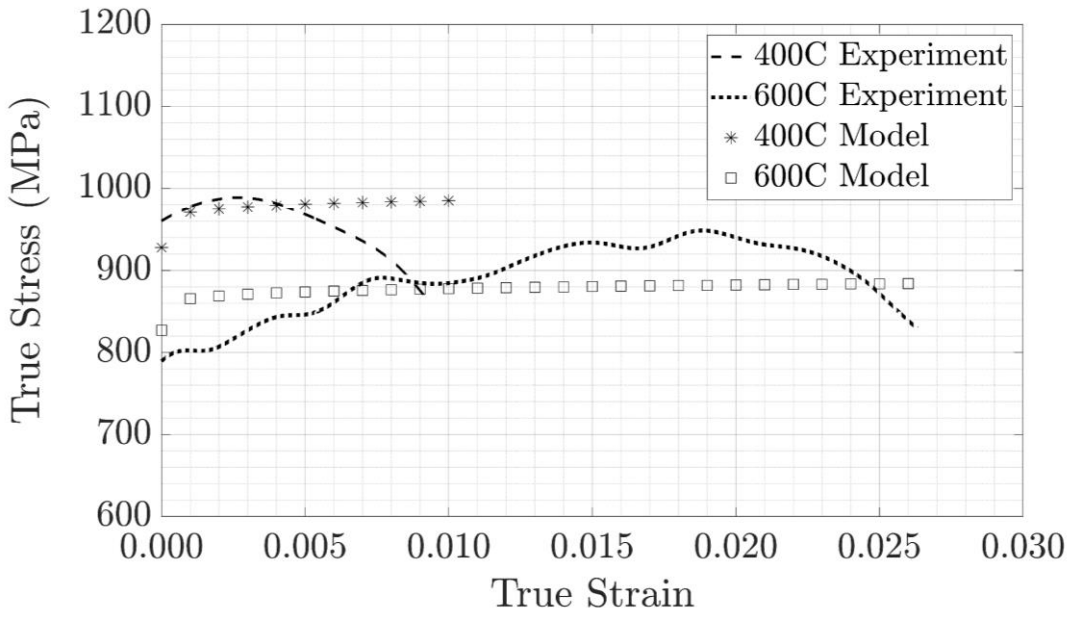

(B)

Fig. 12 Johnson-Cook tensile loading model comparison with experimental data, RT comparison (A) HT comparison (B)

Table 7 Johnson-Cook tensile loading model error analysis

Strain Rate (s^{-1})	Temperature (°C)	Average Relative Error (%)
1000	RT	3.74
2500	RT	4.38
2500	400	7.31
2500	600	5.34
5000	RT	5.89

Conclusions

The dynamic constitutive behavior of H1100 AM 17-4PH SS was investigated under compressive and tensile loading at strain rates ranging from 10^{-3} s^{-1} to 10^{4} s^{-1}. At the average strain rate of 2500 s^{-1}, temperatures ranging from RT to 1000 ºC were investigated for compressive loading, while temperatures ranging from RT to 600 ºC were investigated for tensile loading. Two Johnson-Cook models were developed for this material under these conditions.

The following conclusions were drawn under compressive loading:

- From quasi-static experiments, the compressive yield strength of H1100 AM 17-4PH SS was determined to be 810 MPa and the Young's Modulus was determined to be approximately 150 GPa.
- The material showed strain rate and temperature dependencies. As the strain rate increased from quasi-static (10^{-3} s^{-1}) to 10^{4} s^{-1}, the yield stress increased by 31% and the average flow stress increased by 225 MPa. For the average strain rate of 2500 s^{-1}, as the temperature increased from RT to 1000 °C, the yield strength decreased by 270% and the average flow stress decreased by 700 MPa. Between

600 ºC and 800 ºC, the yield strength of the material was similar. The compression data was similar to that of wrought H1100 17-4PH in tension with respect to yield stress values.

- The compressive Johnson-Cook model was able to predict well for all dynamic strain rates with less than 7% average relative error. Due to the non-monotonically decreasing yield strength and flow stresses of the material between 600 ºC and 800 ºC, the model was not able to predict well for all HT experiments. However, the model was able to predict well for temperatures from RT to 400 ºC with less than 5% average relative error and for 1000 ºC with only 8.64% average relative error. Overall, for RT experiments, the model best predicted at the strain rate of 1000 s^{-1}, with an average relative error of 1.26%. For HT experiments, the model best predicted at 400 °C, with an average relative error of 4.98%.

The following conclusions were drawn under tensile loading:

- From quasi-static experiments, the tensile yield strength of H1100 AM 17-4PH SS was determined to be 625 MPa and Young's Modulus was determined to be approximately 145 GPa, which closely matches the modulus from compression results.
- The material showed strain rate and temperature dependencies. As the strain rate increased from quasi-static (10^{-3} s^{-1}) to 5000 s^{-1}, the yield stress increased by 73% and the average flow stress increased by 475 MPa. The material also showed a low strain-to-failure under quasi-static loading and under dynamic loading. It is postulated that adiabatic heating softened the material during dynamic loading, resulting in a higher strain to failure in dynamic tests than in quasi-static tests. It is

also postulated that the relatively low strain to failure for all tensile tests is the result of porosity. For the average strain rate of 2500 s^{-1}, as the temperature increased from RT to 600 °C, the yield strength decreased by 20% and the average flow stress decreased by 200 MPa.

- The tensile Johnson-Cook model was able to predict well for all dynamic experiments with less than 10% average relative error. For the RT experiments, the model best predicted at 1000 s^{-1}, with an average relative error of 3.74%. For HT experiments, the model best predicted at 600 ºC, with an average relative error of 5.34%.

Acknowledgements

The authors would like to acknowledge ONR Award No. N0014-20-1-2040 and the Naval Undersea Warfare Center (NUWC) Division Newport Chief Technology Office for their generous support of this work. The authors would also like to thank their colleagues at the Dynamic Photo-Mechanics Laboratory for their invaluable discussion.

Appendices

MATLAB Codes

Equilibrium Verification

```
%SHPB Equilibrium Verification

clear all;
close all;

% Parameters

bar_dia = input ('enter bar diameter in m: ');

bar_e = 190e9;
bar_c = 4873;
inc_bar_a = pi*bar_dia*bar_dia/4;
tra_bar_a = pi*bar_dia*bar_dia/4;

%_____________________________________________________________________
__________

% Input from the oscilloscope

data=xlsread('Trial_01.csv');
data=data(1:end,:);
time=data(:,1);
siganl1=data(:,2)*1000*1/1.065;
siganl2=data(:,3)*1000*1/1.065;
siganl3=data(:,4)*1000*1/1.065;
siganl4=data(:,5)*1000*1/1.065;


data_name1(:,1)=time;
data_name2(:,1)=time;
data_name3(:,1)=time;
data_name4(:,1)=time;

data_name1(:,2)=data(:,2);
data_name2(:,2)=data(:,3);
data_name3(:,2)=data(:,4);
data_name4(:,2)=data(:,5);

siganl1(isnan(siganl1))=0;
siganl2(isnan(siganl2))=0;
siganl3(isnan(siganl3))=0;
siganl4(isnan(siganl4))=0;

dt = time(2)-time(1);
```

```
%_____________________________________________________________________
__________

% Balancing signal

signal1_1 = siganl1(1:500,1);
signal2_1 = siganl2(1:500,1);
signal3_1 = siganl3(1:500,1);
signal4_1 = siganl4(1:500,1);
signal1avg = mean(signal1_1);
signal2avg = mean(signal2_1);
signal3avg = mean(signal3_1);
signal4avg = mean(signal4_1);
siganl1 = siganl1 - signal1avg;
siganl2 = siganl2 - signal2avg;
siganl3 = siganl3 - signal3avg;
siganl4 = siganl4 - signal4avg;

%_____________________________________________________________________
__________

% Balancing signal

signal1_1 = siganl1(1:500,1);
signal2_1 = siganl2(1:500,1);
signal3_1 = siganl3(1:500,1);
signal4_1 = siganl4(1:500,1);
signal1avg = mean(signal1_1);
signal2avg = mean(signal2_1);
signal3avg = mean(signal3_1);
signal4avg = mean(signal4_1);
siganl1 = siganl1 - signal1avg;
siganl2 = siganl2 - signal2avg;
siganl3 = siganl3 - signal3avg;
siganl4 = siganl4 - signal4avg;

%_____________________________________________________________________
__________

% Removing bending effect

inc_pulse_originraw = (siganl1 + siganl2) / 2;
tra_pulse_originraw = (siganl3 + siganl4) / 2;

%_____________________________________________________________________
__________

% Filtering signal

fn=0.2;
n=2;

[b,a] = butter(n, fn );
```

```
inc_pulse_origin = filtfilt(b,a,inc_pulse_originraw);

fn=0.05;
n=2;

[bb,a] = butter(n, fn );


tra_pulse_origin = filtfilt(bb,a,tra_pulse_originraw);

%_____________________________________________________________________
_________

% Figures

figure(1),
plot(time*1000000,inc_pulse_origin,'r')
grid on;

figure(2),
plot(time*1000000,tra_pulse_origin,'r')
grid on;


% eval(['t0= ',data_name1,'(1,1)*1000000;'])
 t0 = 1000000*time(1);
beginc=input('please input the time that incident pulse
begins:');
n_inc_begin=ceil((beginc-t0)/(dt*1000000))+1;
n_inc_end=ceil((input('please input the time that incident pulse
ends:')-t0)/(dt*1000000))+1;
n_ref_begin=ceil((input('please input the time that reflected
pulse begins:')-t0)/(dt*1000000))+1;
n_tra_begin=ceil((input('please input the time that transmitted
pulse begins:')-t0)/(dt*1000000))+1;

n0=n_inc_end-n_inc_begin+1;

for i=1:n0
    t(i,1)=(i-1)*dt;
    inc_pulse(i,1)=inc_pulse_origin(n_inc_begin-1+i);
    ref_pulse(i,1)=inc_pulse_origin(n_ref_begin-1+i);
    tra_pulse(i,1)=tra_pulse_origin(n_tra_begin-1+i);


P_inc(i,1)=((inc_pulse(i,1)+ref_pulse(i,1))/1000000)*bar_e*inc_ba
r_a;
    P_tra(i,1)=(tra_pulse(i,1)/1000000)*bar_e*tra_bar_a;
end

figure(3),
plot(time*1000000,inc_pulse_origin,'r');
```

```
hold on;
grid on;
plot(time*1000000,tra_pulse_origin,'b');
grid on; axis tight;
title('Original
pulses','FontName','Timesnewroman','FontSize',12);
xlabel('Time(\mus)','FontName','Timesnewroman','FontSize',12);
ylabel('strain(\mu\epsilon)','FontName','Timesnewroman','FontSize
',12);
legend('Incident Pulse','Transmitted
Pulse','FontName','Timesnewroman','FontSize',12);
%
figure(4)
plot(t*1000000,inc_pulse,'r'),hold on;
plot(t*1000000,-ref_pulse,'g'),hold on;
plot(t*1000000,tra_pulse,'b'),hold on;
axis tight; grid on;
title('Pulses zoom in','FontName','Timesnewroman','FontSize',12);
xlabel('Time(\mus)','FontName','Timesnewroman','FontSize',12);
ylabel('strain(\mu\epsilon)','FontName','Timesnewroman','FontSize
',12);
legend('Incident Pulse','Reflected Pulse','Transmitted
Pulse','FontName','Timesnewroman','FontSize',12);

figure(5)
plot(t*1000000,P_inc,'r.'),hold on;
plot(t*1000000,P_tra,'b'),hold on;
title('Force applied on the
specimen','FontName','Timesnewroman','FontSize',22);
axis tight; grid on;
xlabel('Time(\mus)','FontName','Timesnewroman','FontSize',22);
ylabel('Force(N)','FontName','Timesnewroman','FontSize',22);
legend('Front Face','Back
Face','FontName','Timesnewroman','FontSize',22);
```

Compression Analysis

```
%SHPB Compression Analysis for Maraging Steel Bars

clear all;
close all;

% Parameters

bar_dia = 12.7/1000;

spe_dia=input ('enter specimen diameter in m: ');
spe_l=input ('enter specimen thickness in m: ');

spe_ai = pi*spe_dia*spe_dia/4;
bar_e = 190e3;
bar_c = 4873;
inc_bar_a = pi*bar_dia*bar_dia/4;
tra_bar_a = pi*bar_dia*bar_dia/4;
con = bar_c/spe_l;
%_____________________________________________________________________
__________

% Input from the oscilloscope
data=xlsread('Trial1.csv');
data=data(1:end,:);
time=data(:,1);
siganl1=data(:,2)*1000*1/1.065;
siganl2=data(:,3)*1000*1/1.065;
siganl3=data(:,4)*1000*1/1.065;
siganl4=data(:,5)*1000*1/1.065;

data_name1=data(:,2);
data_name2=data(:,3);
data_name3=data(:,4);
data_name4=data(:,5);

siganl1(isnan(siganl1))=0;
siganl2(isnan(siganl2))=0;
siganl3(isnan(siganl3))=0;
siganl4(isnan(siganl4))=0;

dt = time(2)-time(1);

%_____________________________________________________________________
__________

% Balancing signal

signal1_1 = siganl1(1:500,1);
signal2_1 = siganl2(1:500,1);
signal3_1 = siganl3(1:500,1);
signal4_1 = siganl4(1:500,1);
```

```
signal1avg = mean(signal1_1);
signal2avg = mean(signal2_1);
signal3avg = mean(signal3_1);
signal4avg = mean(signal4_1);
siganl1 = siganl1 - signal1avg;
siganl2 = siganl2 - signal2avg;
siganl3 = siganl3 - signal3avg;
siganl4 = siganl4 - signal4avg;

%_____________________________________________________________________
__________

% Removing bending effect

inc_pulse_origin = (siganl1 + siganl2) / 2;
tra_pulse_origin = (siganl3 + siganl4) / 2;

%_____________________________________________________________________
__________

% Filtering signals

fn=0.2;
n=2;

[bb,a] = butter(n, fn );

inc_pulse = filtfilt(bb,a,inc_pulse_origin);

fn=0.05;
n=2;

[bbc,a] = butter(n, fn );

tra_pulse = filtfilt(bbc,a,tra_pulse_origin);

%_____________________________________________________________________
__________

% Figures

figure(1),
plot(time*1e6,inc_pulse_origin,'r')
title('Input time that the incident and reflected pulse begin and
ends')
grid on;

figure(2),
plot(time*1e6,tra_pulse_origin,'r')
title('Input time that the transmitted pulse begin and ends')
grid on;

t0 = time(1)*1000000;
```

```
beginc=input('Input time that incident pulse begins:');
n_inc_begin=ceil((beginc-t0)/(dt*1000000))+1;
n_inc_end=ceil((input('Input time that incident pulse ends:')-
t0)/(dt*1000000))+1;
n_ref_begin=ceil((input('Input time that reflected pulse
begins:')-t0)/(dt*1000000))+1;
n_tra_begin=ceil((input('Input time that transmitted pulse
begins:')-t0)/(dt*1000000))+1;

pulse_length = n_inc_end - n_inc_begin + 1;

for i = 1: pulse_length
    k1 = n_ref_begin + i -1;
    k2 = n_tra_begin + i -1;
    pulse_time(i,1) = dt*(i-1);
    refl(i,1) = inc_pulse(k1);
    ref_data(i,1)=dt*(i-1);
    ref_data(i,2)=inc_pulse(k1);

    trans(i,1) = tra_pulse(k2);
    tra_data(i,1)=dt*(i-1);
    tra_data(i,2)=tra_pulse(k2);
end

%_____________________________________________________________________
_________
% Area under reflected pulse

rarea(1)=0;
Rfarea(1)=0;
for n=2:pulse_length
    rarea(n)=(refl(n-1)+refl(n))*(0.5*dt);
    Rfarea(n)=Rfarea(n-1)+rarea(n);
end

% Area under transmitted pulse

tarea(1)=0;
TRarea(1)=0;
for n=2:pulse_length
    tarea(n)=(trans(n-1)+trans(n))*(0.5*dt);
    TRarea(n)=TRarea(n-1)+tarea(n);
end

% Engineering, True Stress and Strain, Strain Rate (Compression)

for nn=1:pulse_length
    estrain(nn,1)=-con*(((tra_bar_a/inc_bar_a)-1)*TRarea(nn)-
2*Rfarea(nn))/1e6;
    srate(nn,1)=-con*(((tra_bar_a/inc_bar_a)-1)*trans(nn)-
2*refl(nn))/1e6;
```

```
    estress(nn,1) = -bar_e*(tra_bar_a/spe_ai)*trans(nn)/1e6;
    tstrain(nn,1) = -log(1-estrain(nn,1));
    tstress(nn,1) = estress(nn,1)*(1-estrain(nn,1));
    true_stress_strain(nn,1)=  tstrain(nn,1);
    true_stress_strain(nn,2)= tstress(nn,1);
    e_stress_strain(nn,1)=  estrain(nn,1);
    e_stress_strain(nn,2)= estress(nn,1);
end

%_____________________________________________________________________
_________

%Plots

figure(3)
plot(estrain*100,estress)
xlabel('Engineering Strain
(%)','FontName','Timesnewroman','FontSize',12)
ylabel('Engineering Stress
(MPa)','FontName','Timesnewroman','FontSize',12)
grid on;

figure(4)
plot(tstrain*100,tstress)
xlabel('True Strain
(%)','FontName','Timesnewroman','FontSize',12)
ylabel('True Stress
(MPa)','FontName','Timesnewroman','FontSize',12)
grid on;
title('Pick first point of two points to calculate the slope,
right button to continue');
[x1,y1] = ginput(1);
title('Pick second point of two points to calculate the slope,
right button to continue');
[x2,y2] = ginput(1);
slope = (y2 - y1)*100/(x2 - x1)

title('Press right mouse button to continue, any other to redo')
    [junkx,junky,click]=ginput(1);

figure(5)
plot(pulse_time*1e6,tstrain*100);
xlabel('Time(\mus)','FontName','Timesnewroman','FontSize',22)
ylabel('True Strain
(%)','FontName','Timesnewroman','FontSize',22)
grid on;
%title('Pick first point of two points to calculate the strain
rate, right button to quit');
[x1,y1] = ginput(1);
%title('Pick second point of two points to calculate the strain
rate, right button to quit');
[x2,y2] = ginput(1);
```

```
strainrate = (y2 - y1)/((x2 - x1)*100)*1e6


figure(6)
plot(pulse_time*1e6,srate);
xlabel('Time(\mus)','FontName','Timesnewroman','FontSize',22)
ylabel('Strain Rate (s^-
1)','FontName','Timesnewroman','FontSize',22)
grid on;

%_____________________________________________________________________
__________

% Saving the data

save true.txt true_stress_strain -ascii
save eng.txt e_stress_strain -ascii
```

Tensile Analysis

```
%SHPB Tension Analysis for Maraging Steel Bars

clear all;
close all;

% Parameters

bar_dia = 19.05/1000;

spe_dia=input ('enter specimen diameter in m: ');
spe_l=input ('enter specimen thickness in m: ');

spe_ai = pi*spe_dia*spe_dia/4;
bar_e = 190e3;
bar_c = 4873;
inc_bar_a = pi*bar_dia*bar_dia/4;
tra_bar_a = pi*bar_dia*bar_dia/4;
con = bar_c/spe_l;
%_____________________________________________________________________
__________

% Input from the oscilloscope

data=xlsread('Trial_01.csv');
data=data(1:end,:);
time=data(:,1);
siganl1=data(:,2)*1000*1/1.065;
siganl2=data(:,3)*1000*1/1.065;
siganl3=data(:,4)*1000*1/1.065;
siganl4=data(:,5)*1000*1/1.065;

data_name1=data(:,2);
data_name2=data(:,3);
data_name3=data(:,4);
data_name4=data(:,5);

siganl1(isnan(siganl1))=0;
siganl2(isnan(siganl2))=0;
siganl3(isnan(siganl3))=0;
siganl4(isnan(siganl4))=0;

dt = time(2)-time(1);

%_____________________________________________________________________
__________

% Balancing signal

signal1_1 = siganl1(1:500,1);
signal2_1 = siganl2(1:500,1);
signal3_1 = siganl3(1:500,1);
```

```
signal4_1 = siganl4(1:500,1);
signal1avg = mean(signal1_1);
signal2avg = mean(signal2_1);
signal3avg = mean(signal3_1);
signal4avg = mean(signal4_1);
siganl1 = siganl1 - signal1avg;
siganl2 = siganl2 - signal2avg;
siganl3 = siganl3 - signal3avg;
siganl4 = siganl4 - signal4avg;

%_____________________________________________________________________
__________

% Removing bending effect

inc_pulse_origin = (siganl1 + siganl2) / 2;
tra_pulse_origin = (siganl3 + siganl4) / 2;

%_____________________________________________________________________
__________

% Filtering signals

fn=0.2;
n=2;

[bb,a] = butter(n, fn );

inc_pulse = filtfilt(bb,a,inc_pulse_origin);

fn=0.05;
n=2;

[bbc,a] = butter(n, fn );

tra_pulse = filtfilt(bbc,a,tra_pulse_origin);


%_____________________________________________________________________
__________

% Figures

figure(1),
plot(time*1e6,inc_pulse_origin,'r')
title('Input time that the incident and reflected pulse begin and
ends')
grid on;

figure(2),
plot(time*1e6,tra_pulse_origin,'r')
title('Input time that the transmitted pulse begin and ends')
grid on;
```

```
t0 = time(1)*1000000;

beginc=input('Input time that incident pulse begins:');
n_inc_begin=ceil((beginc-t0)/(dt*1000000))+1;
n_inc_end=ceil((input('Input time that incident pulse ends:')-
t0)/(dt*1000000))+1;
n_ref_begin=ceil((input('Input time that reflected pulse
begins:')-t0)/(dt*1000000))+1;
n_tra_begin=ceil((input('Input time that transmitted pulse
begins:')-t0)/(dt*1000000))+1;

pulse_length = n_inc_end - n_inc_begin + 1;

for i = 1: pulse_length
    k1 = n_ref_begin + i -1;
    k2 = n_tra_begin + i -1;
    pulse_time(i,1) = dt*(i-1);
    refl(i,1) = inc_pulse(k1);
    ref_data(i,1)=dt*(i-1);
    ref_data(i,2)=inc_pulse(k1);

    trans(i,1) = tra_pulse(k2);
    tra_data(i,1)=dt*(i-1);
    tra_data(i,2)=tra_pulse(k2);
end

%_____________________________________________________________________
_____
% Area under reflected pulse

rarea(1)=0;
Rfarea(1)=0;
for n=2:pulse_length
    rarea(n)=(refl(n-1)+refl(n))*(0.5*dt);
    Rfarea(n)=Rfarea(n-1)+rarea(n);
end

% Area under transmitted pulse

tarea(1)=0;
TRarea(1)=0;
for n=2:pulse_length
    tarea(n)=(trans(n-1)+trans(n))*(0.5*dt);
    TRarea(n)=TRarea(n-1)+tarea(n);
end

% Engineering, True Stress and Strain, Strain Rate (Tensile)

for nn=1:pulse_length
    estrain(nn,1)=con*(((tra_bar_a/inc_bar_a)-1)*TRarea(nn)-
2*Rfarea(nn))/1e6;
```

```
    srate(nn,1)=con*(((tra_bar_a/inc_bar_a)-1)*trans(nn)-
2*refl(nn))/1e6;
    estress(nn,1) = bar_e*(tra_bar_a/spe_ai)*trans(nn)/1e6;
    tstrain(nn,1) = log(1+estrain(nn,1));
    tstress(nn,1) = estress(nn,1)*(1+estrain(nn,1));
    true_stress_strain(nn,1)=  tstrain(nn,1);
    true_stress_strain(nn,2)= tstress(nn,1);
    e_stress_strain(nn,1)=  estrain(nn,1);
    e_stress_strain(nn,2)= estress(nn,1);
end

%_____________________________________________________________________
_________

%Plots

figure(3)
plot(estrain*100,estress)
xlabel('Engineering Strain
(%)','FontName','Timesnewroman','FontSize',12)
ylabel('Engineering Stress
(MPa)','FontName','Timesnewroman','FontSize',12)
grid on;

figure(4)
plot(tstrain*100,tstress)
xlabel('True Strain
(%)','FontName','Timesnewroman','FontSize',12)
ylabel('True Stress
(MPa)','FontName','Timesnewroman','FontSize',12)
grid on;
title('Pick first point of two points to calculate the slope,
right button to continue');
[x1,y1] = ginput(1);
title('Pick second point of two points to calculate the slope,
right button to continue');
[x2,y2] = ginput(1);
slope = (y2 - y1)*100/(x2 - x1)

title('Press right mouse button to continue, any other to redo')
    [junkx,junky,click]=ginput(1);

figure(5)
plot(pulse_time*1e6,tstrain*100);
xlabel('Time(\mus)','FontName','Timesnewroman','FontSize',22)
ylabel('True Strain
(%)','FontName','Timesnewroman','FontSize',22)
grid on;
%title('Pick first point of two points to calculate the strain
rate, right button to quit');
[x1,y1] = ginput(1);
```

```
%title('Pick second point of two points to calculate the strain
rate, right button to quit');
[x2,y2] = ginput(1);
strainrate = (y2 - y1)/((x2 - x1)*100)*1e6


figure(6)
plot(pulse_time*1e6,srate);
xlabel('Time(\mus)','FontName','Timesnewroman','FontSize',22)
ylabel('Strain Rate (s^-
1)','FontName','Timesnewroman','FontSize',22)
grid on;

%_____________________________________________________________________
__________

% Saving the data

save true.txt true_stress_strain -ascii
save eng.txt e_stress_strain -ascii
```

Johnson-Cook Model Code

```
% Johnson-Cook Model

close all;
clear all;

% Open figure

openfig('JC Model');
hold on;

% Define strain

ep=0:0.001:0.1;

% Input parameters

A=input('A');
B=input('B');
C=input('C');
n=input('n');
epdot=input('Strain Rate');
T=input('Temperature');
Ts=(T-295)./1378;
m=input('m');

% Plot

sigma=(A+B.*ep.^n).*(1+C.*log(epdot/1000)).*(1-Ts.^m);
plot(ep, sigma);
```

References

1. AK Steel (2018) Armco 17-4PH Stainless Steel. https://www.aksteel.com/sites/default/files/2018-01/17ph201706.pdf. Accessed 10 September 2020
2. Cheruvathur S, Lass E, Campbell C (2016) Additive manufacturing of 17-4 PH stainless steel: post-processing heat treatment to achieve uniform reproducible microstructure. JOM 68: 930–942. https://doi.org/10.1007/s11837-015-1754-4
3. Rafi H, Pal D, Patil N (2014) Microstructure and mechanical behavior of 17-4 precipitation hardenable steel processed by selective laser melting. J. of Material Eng and Perform 23: 4421–4428. https://doi.org/10.1007/s11665-014-1226-y
4. Lum E, Palazotto A, Dempsey A, Abrahams R (2017) Analysis of the effects of additive manufacturing on the material properties of 15-5PH stainless steel. 58th AIAA/ASCE/AHS/ASC Structures, Structural Dynamics, and Materials Conference. https://doi.org/10.2514/6.2017-1142
5. Nezhadfar P, Shrestha S, Phan N, Shamsaei N (2019) Fatigue behavior of additively manufactured 17-4 PH stainless steel: Synergistic effects of surface roughness and heat treatment. International Journal of Fatigue 124: 188-204. https://doi.org/10.1016/j.ijfatigue.2019.02.039
6. Nezhadfar P, Masoomi M, Thompson S, Phan, N, Shamsaei N (2018) Mechanical properties of 17-4 PH stainless steel additively manufactured under Ar and N2 shielding gas. Solid Freeform Fabrication 2018: Proceedings of the 29th Annual International Solid Freeform Fabrication Symposium.

7. Yadollahi A, Shamsaei N, Thompson S, Elwany A, Bian L (2015) Mechanical and microstructural properties of selective laser melted 17-4 PH stainless steel. Proceedings of the ASME 2015 International Mechanical Engineering Congress and Exposition. Volume 2A: Advanced Manufacturing. Houston, Texas, USA. November 13–19. https://doi.org/10.1115/IMECE2015-52362
8. Sun Y, Hebert R, Aindow M (2018) Effect of heat treatments on microstructural evolution of additively manufactured and wrought 17-4PH stainless steel. Materials and Design 156:429-440. https://doi.org/10.1016/j.matdes.2018.07.015
9. Chen W, Song B (2010) Split Hopkinson (Kolsky) Bar: Design, Testing and Applications. Springer, USA
10. Kolsky H (1949) An investigation of the mechanical properties of materials at very
high rates of loading. Proc. Phys. Soc. Sec. B, 62:676-700.
11. Shukla A, Dally J (2014) Dynamic measurements. In : Experimental solid mechanics, 2nd edn. College House Enterprises, USA, pp 513–536.
12. Abotula S, Shukla A, Chona R (2011) Dynamic constitutive behavior of hastelloy x under thermo-mechanical loading. J. Mater. Sci. 46: 4971-4979. https://doi.org/10.1007/s10853-011-5414-y
13. Gupta S, Abotula S, Shukla A (2014) Determination of Johnson–Cook parameters for cast aluminum alloys. Journal of Engineering Materials and Technology 136. https://doi.org/10.1115/1.4027793
14. Nickel Development Institute (1976) 18 per cent nickel maraging steels : engineering properties.

https://www.nickelinstitute.org/media/1598/18_nickelmaragingsteel_engineeringproperties_4419_.pdf.

15. Johnson G, Cook W (1983) A constitutive model and data for metals subjected to large strains, high strain rates, and high temperatures. Proceedings 7th International Symposium on Ballistics: 541-547.

CHAPTER TWO

Manuscript under preparation for journal submission

Dynamic Constitutive Behavior of an Additively Manufactured Nickel-Copper Alloy

C. Fox[1], C. Rousseau[1]*, A. Shukla[1], R. Hebert[2]

[1]*Dynamic Photo-Mechanics Laboratory, Department of Mechanical, Industrial & Systems Engineering, University of Rhode Island, Kingston, RI 02881, USA*
[2]*Department of Materials Science & Engineering, University of Connecticut, Storrs, CT 06269, USA*

*Corresponding Author. E-mail address: roussce@uri.edu; Telephone: 401-874-2542

Dynamic Constitutive Behavior of an Additively Manufactured Nickel-Copper Alloy

C. Fox[1], C. Rousseau[1]*, A. Shukla[1], R. Hebert[2]

[1]*Dynamic Photo-Mechanics Laboratory, Department of Mechanical, Industrial & Systems Engineering, University of Rhode Island, Kingston, RI 02881, USA*
[2]*Department of Materials Science & Engineering, University of Connecticut, Storrs, CT 06269, USA*

*Corresponding Author. E-mail address: roussce@uri.edu; Telephone: 401-874-2542

Abstract

The dynamic constitutive behavior of an additively manufactured (AM) nickel-copper alloy was investigated. An Instron 5582 Universal Tester and a Shimadzu AGX Universal Test Frame were used for quasi-static compression and tension tests, respectively, and a Split Hopkinson Pressure Bar for all dynamic compression and tension tests. High temperature (HT) experiments were conducted using an induction coil heating system. Strain rates of 10^{-3} s^{-1} to 10^{4} s^{-1} were studied. The effects of HT at a strain rate of 2500 s^{-1} were investigated for temperatures ranging from 22 ºC to 1000 ºC for compressive loading, and for temperatures from 22 ºC to 600 ºC for tensile loading.

Keywords

additively manufactured; nickel-copper alloy; Split-Hopkinson pressure bar, high temperature; Johnson-Cook model

Experimental Details

Compressive Quasi-static Characterization

An Instron 5582 Universal Tester is used to determine the compressive quasi-static behavior of the AM nickel-copper alloy at room temperature, 22 °C (RT). The specimen dimensions (see Table 1) and testing procedure are determined from ASTM standard E9-19. During testing a compression rate 1.524 mm/min is used to achieve a strain rate of 10^{-3} s^{-1} up to 25% strain. To reduce interfacial friction between the Instron compression platens and the specimen, molybdenum disulfide is used as a lubricant.

Table 1 Compression specimen dimensions

Strain Rate (s^{-1})	Quasi-static	1000	2500	5000	10000
Diameter (mm)	12.5	6.4	6.4	3.8	3.8
Thickness (mm)	25.4	4.2	4.2	2.5	2.5
Temperature (°C)	22	22	22, 400, 600, 800, 1000	22	22

Compressive Dynamic Characterization

A Split Hopkinson Pressure Bar (SHPB) is used to determine the dynamic behavior of the AM nickel-copper alloy at RT, and at HT's of 400 °C, 600 °C, 800 °C and 1000 °C. Strain rates varying from 10^3 to 10^4 are investigated. The SHPB is comprised of an incident bar, a transmitted bar and a striker bar, all made of 350 maraging steel, as shown in Fig. 1. These bars are aligned along a horizontal axis to ensure uniform specimen deformation and one-dimensional elastic waves during testing.

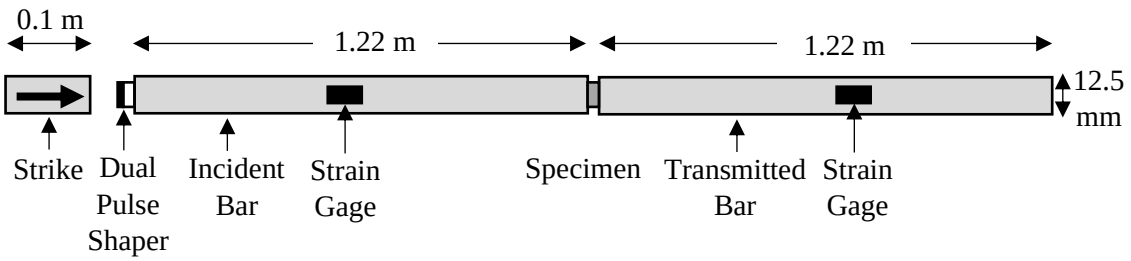

Fig. 1 SHPB compressive loading configuration

Before a test, the cylindrical specimen is positioned between the incident and transmitted bars. The specimen geometry is determined from length to diameter ratios chosen to ensure a state of uniaxial stress, minimal interface friction and reduced specimen inertia in both the radial and longitudinal directions. Table 1 details the specimen dimensions used in this study.

To minimize interfacial friction and prevent barreling, the specimen is well lubricated with molybdenum disulfide for RT tests and with boron nitride for HT tests. To conduct the SHPB test, a gas gun is mounted at the end of the incident bar and fires the striker bar, causing it to impact the incident bar. The striker velocity determines the magnitude of the stress wave, while the striker length determines the pulse length. A pulse shaper is positioned between the striker and the incident bar to optimize the strain profile. This pulse shaper allows for stress equilibrium and constant strain rate in the specimen for the duration of the test. In order to optimize the experiments, a dual copper/steel pulse shaper was used for all strain rates, with the copper (0.375” diameter (9.5 mm), 0.05” length (1.3 mm)) positioned before the steel (0.375” diameter (9.5 mm), 0.25” length (6.4 mm)),, which is affixed to the striker end of the incident bar with petroleum grease. Axial strain gages mounted on the incident and transmitted bars connect to a dynamic signal conditioning

amplifier and oscilloscope system that record the experimental data. Two strain gages are mounted on each bar at least one striker length from the specimen to prevent superposition of the stress waves and at 180^{o} offsets to negate possible bending of the bars. Each strain gage is connected in a quarter Wheatstone bridge configuration.

For the HT tests, the SHPB setup is modified to include an induction coil heating system placed over the specimen, as shown in Fig. 2. Two pumps circulate water through two independent copper coils that are positioned over the ends of the incident and transmitted bars that are in contact with the specimen. This is to prevent a heat gradient in the bars, which would affect their modulus, and thus the wave speed, and to protect the heat-sensitive strain gages. A tungsten carbide insert is placed between the specimen and the incident bar and another between the specimen and the transmitted bar to additionally prevent heating of the bars. The impedance of the tungsten carbide inserts is calculated so as to prevent the compressive stress wave from being altered before reaching the specimen. Therefore, the inserts are 50% smaller in diameter than the incident and transmitted bars. In order to reach the desired experimental temperature in the specimen, calibration experiments are first conducted to determine the relation between induction heating time at certain amperage levels and desired temperature. The calibration relation is developed by spot welding a chromel-alumel thermocouple onto a calibration specimen and its temperature is monitored until the desired temperature is reached and maintained.

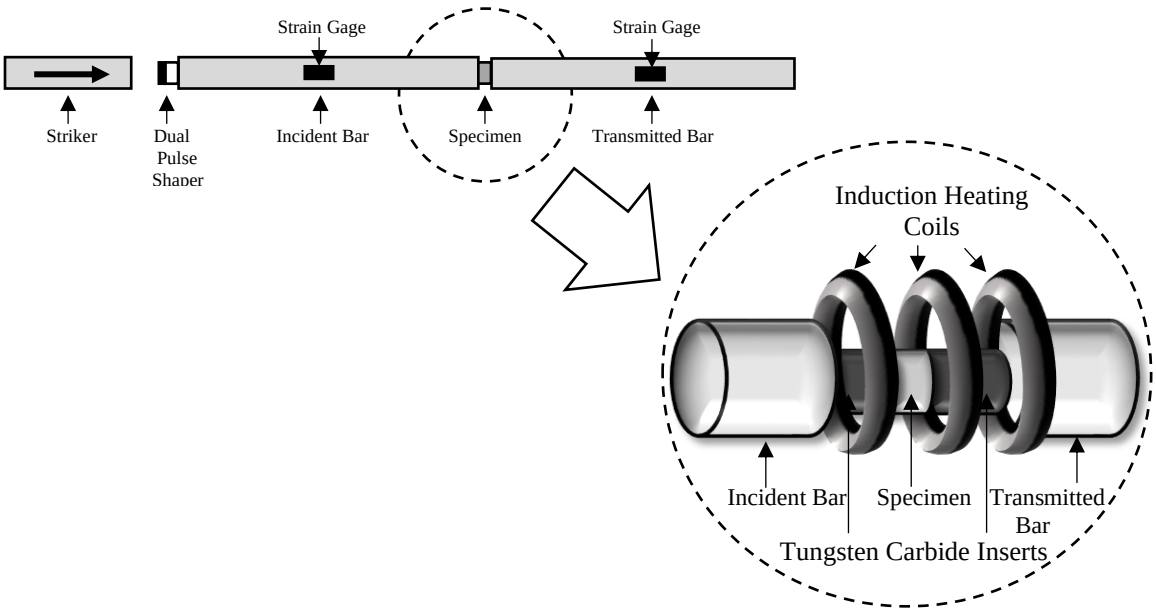

Fig. 2 High temperature compressive SHPB configuration

Tensile Quasi-static Characterization

A Shimadzu AGX Universal Test Frame is used to determine the tensile quasi-static behavior of the AM nickel-copper alloy at room temperature. The specimen dimensions and testing procedure are determined from ASTM standard E8. Strain is recorded using a 1 megapixel camera at a frame rate of 10 fps and a random speckle pattern is applied to the specimen so that 2D Digital Image Correlation could be used to measure strain in the vertical direction.

Tensile Dynamic Characterization

A tensile SHPB setup is used to determine the tensile dynamic behavior of the AM nickel-copper alloy at RT and at HT's of 400 ºC and 600 ºC [13]. Strain rates on the order of magnitude 10^3 are investigated. The tensile SHPB is comprised of an incident bar with a flange on one end, a transmitted bar and a striker, all made of 350 maraging steel. The

incident bar has length 1.22 m, the transmitted bar has length 1.83 m, and the striker has length 0.20 m. Both incident and transmitted bars have diameter 18.8 mm, while the striker fits over the incident bar end and has inner diameter 19.6 mm and outer diameter 31.8 mm. These bars are aligned along a horizontal axis (Fig. 3) to ensure uniform specimen deformation and one-dimensional elastic waves during testing. To hold the specimen, one end of both the incident and transmitted bars have a threaded section of length 16.9 mm, into which the specimen is threaded, completely filling the threaded section and leaving only the gage section of the specimen between the two bars. The setup details are shown in Fig. 3. To conduct a test, the striker is fired from a gas gun positioned over the incident bar, causing the striker to impact the flange, of diameter 41.3 mm and length 39.4 mm, on the end of the incident bar, generating a tensile wave that propagates down to the specimen. The same strain gage configuration and data acquisition system described for compression are used to measure the elastic deformation of the incident and transmitted bars, which allow for calculation of the specimen's stress and strain responses. In order to optimize the tensile tests, much like in the case of compression, a dual pulse shaper is used; however, this time, it is positioned between the striker and the incident flange. It consists of the same copper/steel combination as in the case of compression, but both of the components are now rings that fit over the incident bar and are positioned against the flange. The copper pulse shaper has inner diameter 25.4 mm, outer diameter 38.1 mm, thickness 1.3 mm, and the steel has inner diameter 21.3 mm, outer diameter 38.1 mm, and thickness 2.8 mm.

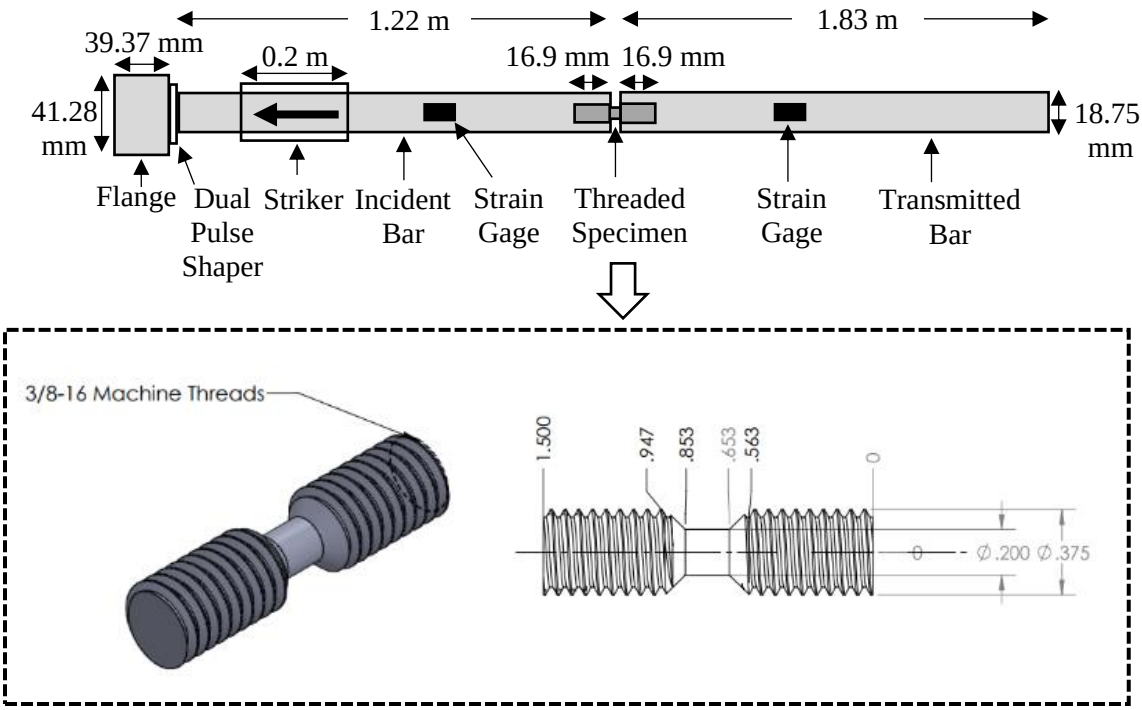

Fig. 3 SHPB tensile loading configuration

Experimental Results

Results will be presented during the oral defense.

Acknowledgements

The authors would like to acknowledge ONR Award No. N0014-20-1-2040 for their generous support of this work.

CHAPTER THREE

Manuscript under preparation for journal submission

Shock Response of Additively Manufactured Nickel-Copper Alloy Corrugated Panels

C. Fox[1], M. Keenan[1], C. Rousseau[1]*, A. Shukla[1], R. Hebert[2]

[1]*Dynamic Photo-Mechanics Laboratory, Department of Mechanical, Industrial & Systems Engineering, University of Rhode Island, Kingston, RI 02881, USA*
[2]*Department of Materials Science & Engineering, University of Connecticut, Storrs, CT 06269, USA*

*Corresponding Author. E-mail address: roussce@uri.edu; Telephone: 401-874-2542

Shock Response of Additively Manufactured Nickel-Copper Alloy Corrugated Panels

C. Fox[1], M. Keenan[1], C. Rousseau[1]*, A. Shukla[1], R. Hebert[2]

[1]*Dynamic Photo-Mechanics Laboratory, Department of Mechanical, Industrial & Systems Engineering, University of Rhode Island, Kingston, RI 02881, USA*
[2]*Department of Materials Science & Engineering, University of Connecticut, Storrs, CT 06269, USA*

*Corresponding Author. E-mail address: roussce@uri.edu; Telephone: 401-874-2542

Abstract

The dynamic response of additively manufactured (AM) nickel-copper alloy corrugated panels is studied using a shock tube. By keeping areal mass density and face sheet dimensions the same for all panels, hexagonal and sinusoidal corrugation geometries are tested to determine the effect of corrugation geometry on shock response. The panels have four layers of corrugation allowing for an equal number of contact points between the corrugations and the face sheets on both the front face (shock side) and back face of the panel, as preliminary tests demonstrated the importance of equal contact. Corrugation buckling and back face panel deflection are tracked using high speed photography and 3D Digital Image Correlation (DIC).

Keywords

shock tube; nickel-copper alloy; 3D DIC; corrugated sandwich panel

Experimental Details

Specimen Details

Corrugated sandwich panels are made from the AM nickel-copper alloy. In order to compare the two different corrugation geometries (sinusoidal and hexagonal) the areal mass density and face sheet dimensions are kept the same for all panels. The panels each have four layers of corrugation allowing for an equal number of contact points between the corrugations and the face sheets on both the front face (shock side) and back face of the panel, as preliminary tests demonstrated the importance of equal contact. Table 1 as well as Figures 1 and 2 detail the specimen dimensions.

Table 1 Specimen dimensions

	Sinusoidal Design	**Hexagonal Design**
Width (mm)	50.80	50.80
Length (mm)	203.20	203.20
Face Plate Thickness (mm)	2.00	2.00
Corrugated Plate Thickness (mm)	0.44	0.44
Total Thickness (mm)	29.35	29.40

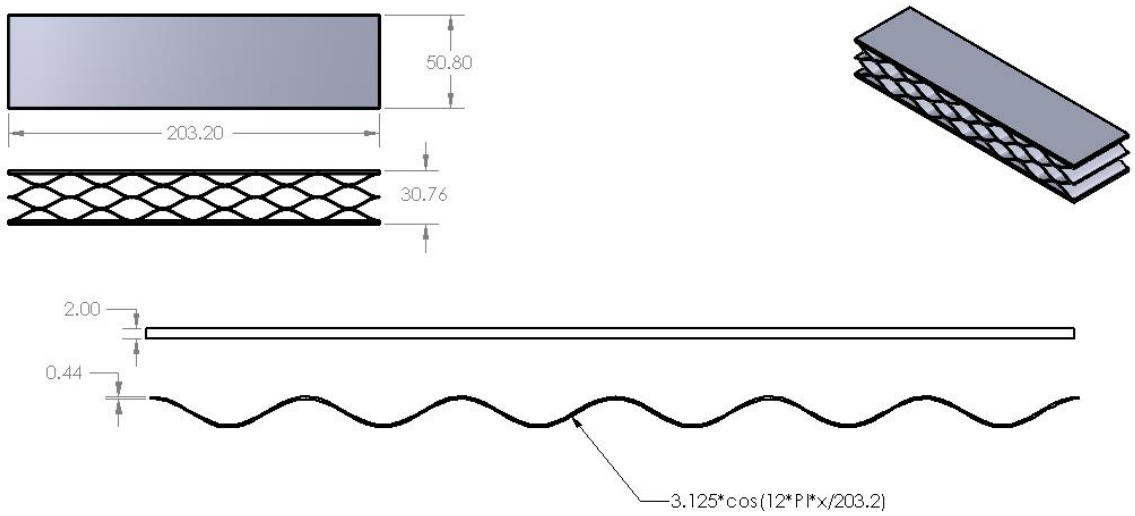

Fig 1 Sinusoidal specimen geometry and dimensions

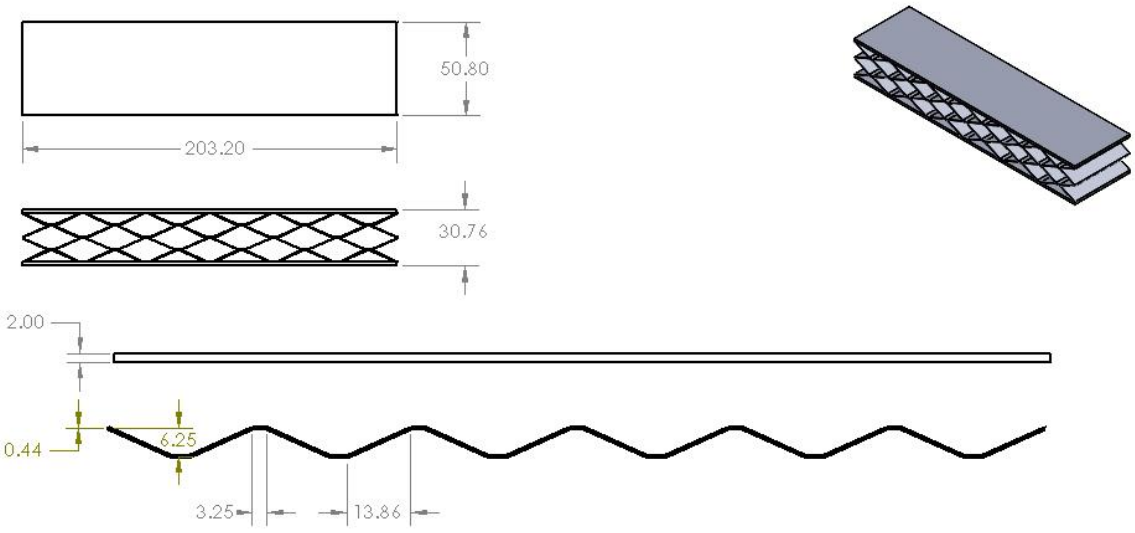

Fig 2 Hexagonal specimen geometry and dimensions

Shock Tube Setup

A shock tube is used to provide planar shock waves to load the corrugated sandwich panels, as shown in Fig. 3. The panels are positioned in a simply supported fixture with a 152.40 mm span and the pressure is applied to the front face of the panel. Piezoelectric pressure

sensors (PCB 113B22 from PCB Piezotronics, Inc., Depew, NY) are located along the specimen end of the shock tube to provide dynamic pressure data of the incident and reflected shock waves. A PCB Piezotronics Model 482C Series sensor signal conditioner and Tektronix DPO 3054 Digital Phosphor Oscilloscope, at a sampling frequency of 250 million samples per second, are used to acquire pressure data. Two high-speed cameras (Photron FASTCAM NOVA S12) with 50 mm lenses are positioned to view the back face of the specimen, which has a random speckle pattern for 3D DIC. The cameras are positioned with an angle of 22 degrees between their lines of sight and framing rate of 30,000fps is used to provide an image resolution of 768 by 560 pixels. A calibration grid is manually displaced at the specimen location and images are taken in all degrees of freedom. The 3D DIC calibration is completed using VIC-3D 8 software (Correlated Solutions, Inc., Columbia, SC).

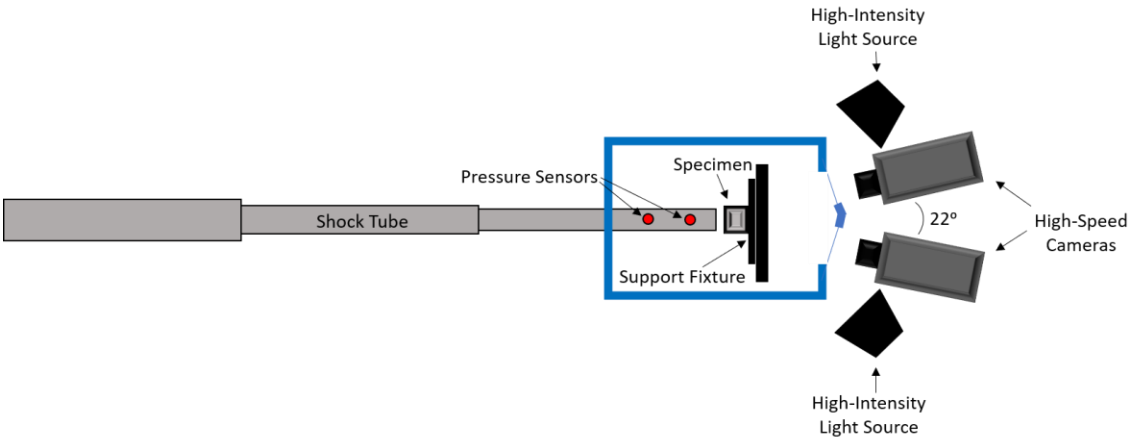

Fig 3 Shock tube configuration (top view)

Experimental Results

Results will be presented during the oral defense.

Acknowledgements

The authors would like to acknowledge ONR Award No. N0014-20-1-2040 for their generous support of this work.